Winter 12-14-2019

Expanding the Palette: Synthesizing Microencapsulated Organic Phase Change Materials in Metallic Matrices for Transient Thermal Applications

Melissa Kate McCann
Washington University in St. Louis

Washington University in St. Louis

McKelvey School of Engineering

Department of Material Science and Mechanical Engineering

Thesis Examination Committee:

Damena Agonafer, Chair

Katharine Flores

Julio D'Arcy

Michael Fish, ARL Advisor

Lauren Boteler, ARL Advisor

Expanding the Palette: Synthesizing Microencapsulated Organic Phase Change Materials in Metallic Matrices for Transient Thermal Applications

By

Melissa Kate McCann

A thesis presented to the McKelvey School of Engineering of Washington University in St. Louis in partial fulfillment of the requirements for the degree of Master of Science.

December 2019

St. Louis, Missouri

Acknowledgements

To everyone at the Army Research Laboratory, thank you for your guidance throughout the project and the opportunity to work alongside many brilliant scientists. In particular, I would like to extend my thanks to Dr. Lauren Boteler for broadening my understanding of the project's real-world applications. Without her, this project wouldn't have been possible. My gratitude is deeply felt for both Dr. Michael Fish and Mr. Morris Berman for your unparalleled programming knowledge and patience. Mike, I am thankful for our thoughtful conversations and I am glad you adopted this project. Dr. Adam Wilson, you have taught me so much about TDTR. Thanks for answering all of my questions regarding this process. Thank you to Mr. Claude Pullen for all of your technical advice and ability to keep a smile on my face every day. I am grateful for my summer 2019 research experience and all of the support I have had from my colleagues at ARL.

Dr. Damena Agonafer, thank you for supporting this project here at Washington University in St. Louis. Your commitment to a detailed report has pushed me to put forth my best efforts throughout this writing process.

To my parents, this accomplishment isn't just mine, it is yours too. Thanks for always supporting my endeavors, even if it requires me to constantly pursue research opportunities far away from home. I am proud to be your favorite, and only, daughter.

To my uncle Keith, you have aided in my education endeavors in so many ways and I can never thank you enough for your support and guidance.

Finally, to my boyfriend, Eli, your unyielding encouragement has been amazing. Thanks for always being the person I rely on the most to get through both the stressful and the exciting times.

Table of Contents

List of Tables

List of Figures

Abstract

Expanding the Palette: Synthesizing Microencapsulated Organic Phase Change Materials in Metallic Matrices for Transient Thermal Applications

By

Melissa Kate McCann

Master of Science in Materials Science & Engineering

Washington University in St. Louis, 2019

Research Advisor: Professor Damena Agonafer

As the demand for smaller and faster electronics increases, it becomes increasingly challenging to effectively manage the generated heat without hindering device performance in applications whose thermal profiles are dominated by pulsed thermal loads. Heat propagation in a system can be characterized by steady or transient state heat transfer. In steady state, the temperature at any particular point remains constant after thermal equilibrium is reached. In a transient state, the temperature within a system varies over time. The changing parameters and time dependency associated with a transient regime make heat transfer calculations far more complex than in a steady state. Thus, many electronic devices are designed for steady state operation under peak loading conditions and the associated increased temperatures. However, these peak conditions occur infrequently, leading to unnecessary system overdesign.

Phase change materials (PCMs) are heat mitigation materials for transient conditions. These materials can maintain a nearly constant temperature during the phase transformation of pure or eutectic substances, which are used as thermal buffers in electronic devices, especially in

applications with intermittent loading profiles or transient power spikes. This work specifically focuses on organic and metallic PCMs. Organic PCMs are characteristically lightweight, have a high specific latent heat, and are inexpensive. Despite these advantages, low thermal conductivity limits their widespread application. As an alternative, metallic PCMs have high volumetric latent heat and thermal conductivity values. This study introduces a new concept of combining the two PCMs into a material composite that exploits the advantageous physical characteristics and thermal properties of each material for specific transient thermal electronic applications.

This research aims to mitigate the overdesign of electronic packaging by incorporating melamine microencapsulated paraffin spheres embedded in a Field's metal (32.5Bi/51In/16.5Sn wt%) matrix to dissipate heat. Four PCM concentrations are synthesized, with paraffin volumetric fractions of 21.8%, 40.3%, 50.1%, and 61.2%. The collected data is compared to distinct organic and metallic PCM performance records available in the literature. The results can guide future innovative composite studies.

To characterize the PCM composites, differential scanning calorimetry (DSC), scanning electron microscopy (SEM), micro-computed tomography (micro-CT), and time-domain thermoreflectance (TDTR) techniques are employed. Manual mixing most effectively combined the two PCMs after particle dispersion analysis in comparison to the other combination techniques. The physical experiments are validated by computer-modeled simulations. An explicit model of a dynamic system is created to characterize the interactions between the size of the particles, heat flux, and temperature propagation. The computer model provides insight into the material characteristics and interactions that facilitate predicting specific trends at various temperatures. In a high pulse rate scenario, with time scale matching, the onset of the steady state

regime in a transient system is delayed by approximately 50%. The novel PCM fabrication approach presented here decreases the device package size, limits the associated weight, increases the system performance, and minimizes the composite cost (SWaP-C). The synthesized composites have enormous potential for cooling specific electronics-based applications due to the organic to metallic PCM ratio, tailorable material properties, and application-specific phase change onset temperature. This study provides a new foundation for future composite research that maximizes the advantages of systematically combining organic and metallic PCMs.

Chapter 1: Introduction and Motivation

Thermal Energy Challenges

Enhanced functionality and size reduction of electronic devices has led to a rapid increase in device power density. Specifically, an increased demand in overall performance has resulted from the miniaturization of circuit components, the reduction in associated costs, and the increased mobility of electronic devices[9]. However, a potential thermal bottleneck has developed due to the unchanged limits of the thermal components. It has become increasingly challenging to effectively manage the generated heat without hindering device performance. Since the conventional way of removing heat with liquids has reached its limit due to the low thermal conductivity and heat capacity values of fluids, a proposed solution to mitigate the overdesign of packaging applications is to incorporate heat dissipating materials[14]. This study incorporates materials with large latent heat of fusions to increase the heat capacity of the device and improve the overall heat propagation in the system.

Transitioning from Steady State to Transient State

Many electronic devices require short bursts of high computational demand interspersed with periods of lower demand, which leads to designing for responsiveness rather than sustained performance[9]. As a result, devices are intended for steady state solutions, which focus on peak loading conditions. In steady state, the temperature at any particular point remains constant after thermal equilibrium is reached. Typical steady state thermal solutions focus on better heat sinks and high thermal conductivity materials. This study introduces a transient thermal solution for pulsed thermal loads. In a transient state, the temperature within a system varies over time. By implementing a system capable of providing sufficient cooling capacity during the various loading conditions and dissipating that heat prior to onset of another thermal event, the system

can be designed for a capacity closer to the average thermal power level rather than the peak[4]. For transient applications, a fundamental shift in thermal/packaging technology is required. This specifically addresses the pulsed nature of the application. The changing parameters and time dependency associated with a transient state do make heat transfer calculations far more complex than in a steady state. This is why many electronic devices are designed for steady state operation under peak loading conditions and the associated temperatures.

Another design parameter to consider is the thermal energy storage process. The most common, simple, low-cost, and longstanding technique is the sensible heat method. In this case, the storage medium temperature shifts without phase change because the sensible heat content increases as the temperature rises[3]. In general, the gain in heat is accompanied by a change in either the volume or pressure.

Material Thermal Parameters

This study deviates from the traditional sensible heat storage method. A much higher storage density and a smaller temperature difference when storing and releasing heat was exhibited with the incorporation of phase change materials (PCMs)[14]. In relation to the transient thermal approach, the temperature conditions are averaged, and the system is designed to perform at the mean loading conditions due to the introduction of PCMs.

Solid-to-liquid PCMs adsorb thermal energy during phase changes without a rise in temperature due to their isothermal properties. The large absorption of latent heat compared to heat capacity is promising for thermal energy storage and heat transfer[16]. Latent heat is the energy absorbed or released by a thermodynamic system during a constant temperature process. An example of this process includes ice melting or water boiling. It is the basic phase change when a solid substance turns into a liquid (melts) or a liquid substance transitions into a gas

(evaporation). Due to the high storage capacity and small temperature variation from storage to retrieval, latent heat has proved to be an effective storage means for thermal management[36]. In order to quantify the advantages of the described design and material choices, a timescale matching concept was employed to physically compare the increased performance of the PCMs to traditional materials.

The remainder of this chapter will discuss the types of PCMs currently researched. This includes the specific application incorporation and material modifications for organic and metallic PCMs. The advantages of the PCM composite that this study researched will be presented based on the SWaP-C criteria. The PCM composite's novel mixing technique will be explained along with the potential application niches. Finally, the research hypothesis and scientific contributions will be outlined.

Timescale Matching Concept

Boteler et al. (2019) investigated various testing conditions to improve electronic devices system size and weight without sacrificing performance by developing a package focused on transient thermal mitigation using timescale matched (TSM) PCMs. This concept relies on the multiple PCMs working together in a system to dissipate heat. The TSM PCMs included organic PCMs in conjunction with metallic PCMs to compare the benefits of each material. Timescale matching allows the high thermal conductivity of metallic PCMs to quickly absorb the initial portion of the pulse, which is referred to as the primary melt. In comparison, the slower heating of the low thermal conductivity organic PCMs is delayed and reaches its melt front during the secondary melt stage of the pulse[4]. The concept of TSM was presented as well as a numerical study outlining design trade-offs, packaging considerations, and the TSM regimes. It was found that for short pulses, metallic PCMs have a fast-thermal response due to their high thermal

conductivity but their weight, cost, and integration complexity limits their viability in applications. Thus, complete metallic PCM systems are not the most efficient and advantageous material for pulsed thermal loads. The placement and concentration of organic PCMs is important, as well.

From the specific TSM regimes, heat dissipating materials can to be customized to accommodate the thermal profiles between the trade space of the application. Designing solutions to effectively transfer heat into the organic PCM through the metallic PCM can effectively lower the weight while allowing performance tradeoffs determined by the maximum temperature threshold. It is necessary to determine the correct configuration of materials for the pulse application of interest.

Phase Change Material (PCMs)

In general, PCMs are associated by three energy storage methods: sensible heat, latent heat, and chemical energy. There are numerous types of PCMs including: metals, salt hydrates, fatty acids, esters, polyethylene glycols, paraffin, and many more. From this expansive list, the vast majority of PCMs fall into three main classifications: organics, inorganics, and liquid metals.

Depending on the application, a PCM is selected based on its melting point. PCMs dissipate heat generation and are widely studied due to their ability to absorb thermal energy with minimal temperature increase during phase change (solid-liquid) of pure or eutectic substances[11]. Electronics have benefitted by using PCMs as thermal buffers, especially those applications with intermittent loading profiles or transient power spikes[10].

The current study expands upon these thermal and physical properties by incorporating a microencapsulated organic PCM into a metallic PCM to create a PCM composite. The objective was to determine the effectiveness of using a metallic PCM with an embedded spherical organic

PCM to passively reduce temperature during high rate transient pulses. A PCM composite can help bridge the gap between the properties of the organic and metallic PCMs. The phase transition (solid-liquid) temperatures are specifically chosen to occur within the desired application range. The combination of the two PCMs disclose niche applications, which incorporate the advantageous properties of each PCM. By integrating PCMs with electronic packages, the overall system can be improved by reducing the heat sink and cooling requirements or increasing dissipated power density, while at the same time, ensuring the device temperature does not exceed its limit under pulsed loading conditions[4].

Encapsulated Organic PCMs

Organics are the most commonly researched PCM[10]. Waxes, specifically, are lightweight, have a high specific latent heat, and are inexpensive. To mitigate changes in the wax volume during phase transition, supercooling, and low thermal conductivity values, microencapsulation of organic PCMs has been investigated[13]. Generally, microencapsulated PCMs provide portable heat storage and transfer system with the additional protective shells around the particles [14]. Hawlder et al. (2002) encapsulated paraffin wax in a packed bed heat exchanger. The designed experiments were based on surface response method, to optimize the processing conditions. The authors found that a higher coating to paraffin ratio led to an increased paraffin encapsulation ratio. Thermal cycling tests showed that encapsulated paraffin maintained its original geometrical profile and energy storage capacity after 1000 cycles.

PCMs are also encapsulated in a micro sized sphere for containment during the liquid state. When determining the shell material's compatibility with the interior PCM, the shell itself should have a higher melting point than the PCM core and be able to maintain a spherical shape under mechanical and thermal stresses. The encapsulate material should have good thermal

conductivities and undergo minimal super-cooling. Preventing interior PCM leaking upon melting is a critical function of the shell encapsulate. Otherwise, agglomeration of the PCM can occur, which causes a temperature delay in the following melting cycle[13]. A non-melting ceramic or polymer shell can be made around small PCMs particles to form encapsulated phase change units[14].

Combined Organic PCM Systems

Another method to increase the thermal conductivity of organic PCMs is to supplement them with other structures or materials that have advantageous thermal properties. Various methods have been proposed to enhance the heat transfer in a latent heat thermal system, with metallic fillers, metal matrix structures, and aluminum shavings to improve the organic PCM's thermal conductivity. For a metallic filler, Zhao et al. (2010) embedded metal foams to enhance the PCM heat transfer by relying on the melting phenomenon where natural convection can improve the heat transfer performance of the PCM. This reduces the temperature difference between the heated surface and the material. The authors found that depending on the metal foam structure and materials, this material can increase the overall heat transfer rate by 3–10 times during the melting process (two-phase zone) and the pure liquid zone.

Xie et al. (2015) combined a shape-stabilized PCM with an aluminum honeycomb, which was intended to enhance the thermal conductivity and structural strength of the organic PCM, while contributing little additional weight to the system. The shape-stabilized PCM was made of paraffin, high density polyethylene, and expanded graphite. The study showed that addition of the aluminum honeycomb structure limited the range of the temperature variation of the heating source, compared to the same conditions without the structure. The thermal conductivity of the PCM–honeycomb composite structure was enhanced to 2.08 W/m K.

Liu et al. (2005) created a metal fin structure comprised of an electrical heating rod and an outer tube, with the in-between space of the annulus filled with stearic acid. The fin was designed and fixed to the electrical heating rod to enhance the thermal response of the stearic acid. The experimental results show that the fin improved the heat transfer of the melting process of the thermal storage unit by an augmented factor up to 3 compared to the equivalent thermal conductivity of the PCM.

Metallic PCMs

Alternatively, to organics, metallic PCMs have advantageous thermal properties with high values in volumetric latent heat and thermal conductivity. These materials have been presented as having a promising high heat fluxes, being compact, and having fast action times for thermal solutions were system weight is less of a concern compared to high heat transfer rates[10,15]. Despite their seemingly ideal fit for faster transient loads, few studies have been published using metallic PCMs. Of these, only some studies consider short timescales that would take advantage of the high heat rates enabled by metallic PCMs, and the majority of those are only simulations[10].

Krishnan & Garimella (2004) performed a transient thermal analysis to compare the use of PCMs and solid copper heat sinks for two different pulsed heat input levels of 600 W for 25 s and 300 W for 50 s. Four different PCMs including two metallic alloys, an organic material, and an organic material imbedded inside a metal foam were studied to explore possible usage trade-offs. It was shown that the performance of the metallic PCMs and an organic PCM with a thermal conductivity enhancer can be comparable depending on the characteristics of the foam in question[17]. The performance of an organic and metallic PCM combination was not tested.

PCM Composite SWaP-C Advantages

The advantages to the novel PCM fabrication approach presented in this study decreases the device package size, limits the associated weight, increases the system performance, and minimizes the composite cost (SWaP-C). The system size is decreased from the transition from a steady state design to a transient thermal configuration by focusing on the average loading conditions. This reduces the cooling overdesign of the system and the weight is reduced in comparison to a fully metallic PCM. As shown in Table 1, the weight of the PCM composite is reduced due to the increased concentration of the organic PCM denoted by the five volumetric fractions. The 0.0% concentration is a fully metallic sample of Field's metal, which served as a baseline for subsequent composite samples. The calculations supporting Table 1 can be found in Appendix A.

Table 1. Weight comparison reduction chart determined by the concentration of organic PCM (microencapsulated paraffin wax). Due to the lower density of the organic PCM, the overall weight of the heat dissipating material was reduced in comparison to a fully metallic PCM sample.

Weight Comparison	
Encapsulated Paraffin Wax Concentration	Weight Reduction
0.0%	0.0%
21.8%	19.4%
40.3%	35.8%
50.1%	44.5%
61.2%	54.4%

The application's system performance is increased due to the combination of the advantageous properties from both types of PCMs, specifically the lower density of the organic PCM and higher thermal conductivity of the metallic PCM. The thermal properties increase due to the addition of metallic PCM in an otherwise all organic system.

The cost is also reduced in comparison to a purely Field's metal system. The cost reduction was calculated summarily to the methods for the weight reduction calculations. In Table 2, the cost of each PCM was determined by the physical materials purchased from their respective vendors. The microencapsulated paraffin powder had an overall lower cost, thus the PCM composites with the higher concentrations of organic material had an overall higher percent cost reduction. The calculations supporting Table 2 are available in Appendix B.

Table 2. Cost comparison reduction chart determined by the concentration of organic PCM (microencapsulated paraffin wax). Due to the lower cost of the organic PCM, the overall cost of the heat dissipating material was reduced in comparison to a fully metallic PCM sample.

Cost Comparison	
Encapsulated Paraffin Wax Concentration	Weight Reduction
0.0%	0.0%
21.8%	21.6%
40.3%	40.0%
50.1%	49.7%
61.2%	60.7%

This study investigated the fabrication of PCM composites to improve the system size, weight, and cost without sacrificing performance based on the transient thermal mitigation.

Novel Mixing Concept

The original intention of mixing the organic and metallic PCMs was to create a uniform, cubic-close packed structure. With this orientation, creating computer simulations would be facilitated due to the linear and easily replicable design. Figure 1 depicts the orientation of the organic spheres in one cubic dimension of Field's metal.

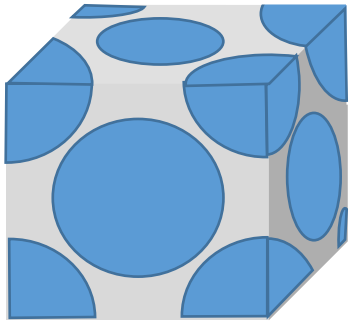

Figure 1. The cubic-close packed structure represented by the microencapsulated paraffin particles (blue) and the Field's metal (gray).

In order to create a procedure that was easily replicable, could scale with varying quantities of each composite, was inexpensive, and provided consistency between samples, four techniques were investigated. These techniques ranged from simple manual mixing, a floating particle uniform orientation study, the use of a non-contact planetary mixing centrifuge, and drop casting. The mixing technique used met all of the initial criteria of simplicity and dispersion of paraffin particles.

Manually mixing the two materials together proved to be the most effective method to create the composite material. The mixing preparation and device set-up simply included a hot

plate set to ~75°C, a wooden stirrer, a mixing dish, and a scale to record the sample weight. A uniform, cubic-close packed structure was not obtained from this method. Two particle dispersion studies and corrections in the modeling depicted the orientation of the paraffin particles embedded in the metallic PCM substrate.

Application Niches

Around the world, direct solar radiation is considered to be one of the most prospective sources of energy. However, large-scale utilization of solar energy is possible only if the effective technology for its storage can be developed[1]. One of the prospective techniques incorporates PCMs due to their ability to store thermal energy for effective use in passive and active solar space heating systems, greenhouses, and solar cooking[16]. Sharma et al. (2009) discuss the vast application space where PCMs can be incorporated including, buildings materials for wallboards, shutters, under-floor heating systems, and ceiling boards.

Ganatra et al. (2018) investigated the feasibility of a passive cooling system based on PCMs for thermal management of mobile devices. Through experimentation, key parameters were evaluated to determine the design include of a PCM based thermal management system. A significant extension in the time that the processor could run at full power before the processing power would need to be throttled to prevent damage was found in the mobile device application[9].

The military has various high rate transient pulse applications which create unique thermal management challenges due to their high heat flux and short pulse duration[10]. This is particularly true for high pulse rate laser applications. The PCM composite study for this thesis project was created with this military application in mind.

Research Potential

The research inquiries driving this thesis work were to determine if an organic and a metallic PCM can be effectively combined to create a composite that could be characterized physically and computationally, be supported with computer simulations, and could quantitively outperform traditional PCM materials based on a heat propagation comparison in a high pulse rate transient system. If a synthesized composite can be fabricated and effectively characterized, then there is enormous potential for cooling specific electronics-based applications. This is due to the organic to metallic PCM ratio, tailorable material properties, and system-specific phase change onset temperature. The concentration of the organic PCM can be adjusted based on constraints related to the overall composite cost or weight. PCM composites would be able to be chosen based on their thermal and physical properties for the specific application, paying particular attention to the temperature system range.

Contributions

For the scientific community contribution, this PCM composite fabrication study is the first to combine an organic and metallic PCM together in current existing literature. A manual mixing process was proven to be the appropriate material combination technique through supported particle dispersion and homogeneity studies (Chapter 2). The orientation of the paraffin spheres was confirmed through both topological characterization with scanning electron microscopy and a cross-section analysis with micro-computed tomography using analyzed area calculation yields (Chapter 3).

Since thermal conductivity values for the Field's metal and organic PCM composites were not readily available in literature, this study provides values from an employed thermo-analytical technique (Chapter 4). The measurements from the TDTR systems confirm the

thermal conductivity for Field's metal is 18.0 W/m K. For the composite systems of 21.83% and 40.32% encapsulated paraffin wax concentrations, the measured thermal conductivities are 15.6 W/m K and 7.0 W/m K, respectively. From the assigned thermal conductivity values, an explicit system of the composite material was effectively modeled (Chapter 5). These values can be supplemented in future work with a two-temperature finite difference model (Chapter 6). This is the first known model for an organic and metallic PCM composite.

Chapter 2: Materials and Mixing Techniques

Phase Change Materials Introduction

This research project determined the physical distribution of spherical organic phase change materials inside a metallic substrate. The microencapsulated organic materials were purchased from Microtek Laboratories, Inc. The product Nextek^{TM} 58D (T_m ~ 58°C) was purchased in a dry powder form. As shown in Figure 2, the dry powder was a white precipitate with a flour-like consistency, which was kept covered to prevent airborne particle dispersion during transport and experimentation.

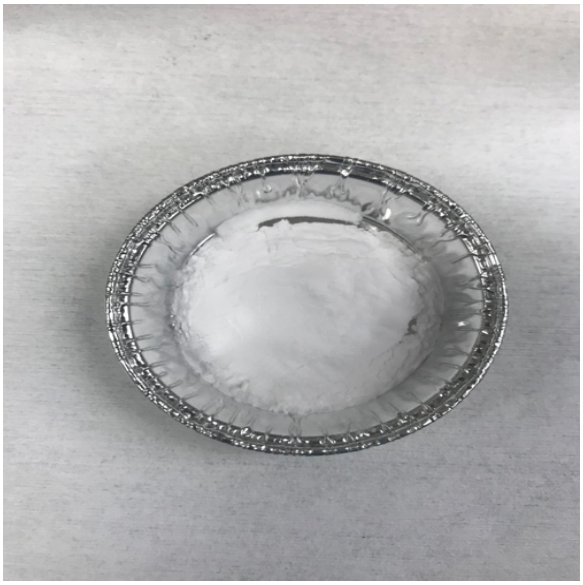

Figure 2. The organic PCM dry powder in an aluminum weigh dish.

Paraffin wax was the encapsulated organic material chosen for this study because it has a high latent heat of fusion, is chemically inert, has no phase segregation, and is commercial availability at a low cost[36]. Paraffinic hydrocarbons, or paraffins, are straight-chain or branched saturated organic compounds with a C_nH_{2n+2} composition. The term paraffin wax relates to mixtures of various hydrocarbon groups, especially paraffins and cycloalkanes, which are solid

at ambient temperatures[8]. The properties for the paraffin wax in this study correlate to two solid paraffin hydrocarbons: heptacosane ($C_{27}H_{56}$) and hexacosane ($C_{26}H_{56}$).

According to the supplier, the PCM comprised approximately 87% of the microcapsules' mass, while the polymer wall comprised 13%. As shown in Figure 3, the interior of each sphere consisted of paraffin wax, an organic PCM. The capsule wall of each particle was a modified melamine ester chemistry which decomposes at its melting temperature of 345°C. As a monomer for making thermosetting resin, melamine is combined with a formaldehyde (CH_2O) and cross-linking agents for coating materials[27]. An ester is an organic compound where the hydrogen in the compound's carboxyl group is replaced with a hydrocarbon group. Esters are most commonly derived from carboxylic acids[5]. According to the manufacturer, the wall thickness was approximately 0.3 µm and the mean pristine particle size was 15-30 µm. The particles, as received, had no surface functionalization and no additional secondary processes were incorporated to functionalize the surface during the study.

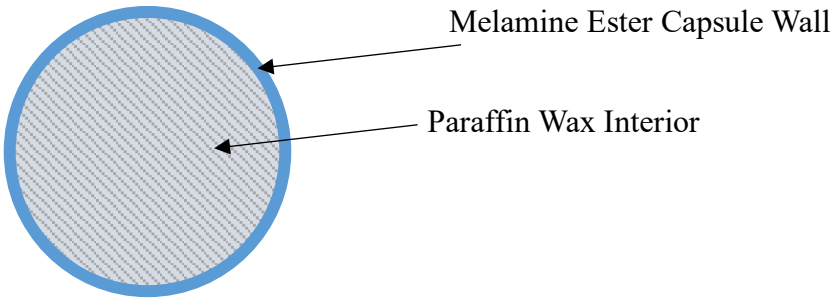

Figure 3. The interior of each organic particle is paraffin wax (solid-liquid PCM) and the outer shell is a melamine ester (~0.3 µm).

For this study, the melamine microencapsulated paraffin spheres were dispersed within Field's metal (32.5Bi/51In/16.5Sn wt%) samples. The metallic PCM was purchased from

Rotometals, Inc. The Field's metal was Roto144F Low Melt Fusible Ingot Alloy (T_m ~ 59°C). Field's metal is a fusible alloy, which melts at relatively low temperatures. The Field's metal is created by a homogeneous, eutectic mixture of bismuth, indium, and tin constituents that melt or solidify at a single temperature that is lower than the melting point of any of the individual constituents or any other possible mixing ratio. Eutectic substances nearly always melt and freeze without segregation since they freeze to an intimate mixture of crystals, leaving little opportunity for the components to separate. During melting both components liquefy simultaneously, making separation unlikely[26]. Field's metal was specifically chosen due to its low melting temperature and eutectic properties.

Each individual PCM and composite sample was weighed with a Mettler Toledo XP26. The composites were fabricated based on the associated mass percentage of each constituent material. The presence of organic to metallic material determined the labeled mass percentages of 3.0%, 7.0%, 10.0%, and 15.0%. The percent organic mass values were converted to volumetric fractions to facilitate comparison with values in the literature. The volumetric fractions were derived by multiplying the mass of each of the materials and the density of either Field's metal or the powder. Each of these calculations is shown explicitly in Tables 3-5. The density of Field's metal is 7880 kg/m^3, according to the Rotometals, Inc data sheet. The effective density of the organic spheres was calculated from the average densities of heptacosane (787 kg/m^3) and hexacosane (785 kg/m^3), with the additional density of melamine (1570 kg/m^3). The powder's effective density was calculated to be 876 kg/m^3. The volume (V) was found by dividing the weighed mass (m) by the calculated density (ρ):

$$V=m/\rho\ .$$

The volume fraction (V_f) is the powder volume (V_p) divided by the Field's metal volume (V_{fm}) plus the powder volume:

$$V_f = \frac{V_p}{V_{fm}+V_p}.$$

Within these calculations, the mass percentages of 87% paraffin and 13% melamine per pristine capsule was incorporated into the effective density of the powder. The melamine ester capsule wall remains intact throughout the experiment, however the organic PCM will be referred to as a paraffin sphere throughout the remainder of this text for simplicity. These volumetric fractions were used to identify the composite concentrations throughout the study. The values were confirmed by a particle dispersion study.

Table 3. Field's metal mass to volume conversion chart.

Field's Metal Mass to Volume Conversion			
Paraffin Concentration by Mass Percentage (%)	Field's Metal Mass (kg)	Field's Metal Density (kg/m^3)	Field's Metal Volume (m^3)
3.00	$9.75*10^{-3}$	7800	$1.24*10^{-6}$
7.00	$9.35*10^{-3}$	7800	$1.19*10^{-6}$
10.00	$9.01*10^{-3}$	7800	$1.14*10^{-6}$
15.00	$8.56*10^{-3}$	7800	$1.09*10^{-6}$

Table 4. Paraffin powder mass to volume conversion chart.

Paraffin Powder Mass to Volume Conversion			
Paraffin Concentration by Mass Percentage (%)	Paraffin Mass (kg)	Paraffin Density (kg/m^3)	Paraffin Volume (m^3)
3.00	$3.03*10^{-4}$	876.00	$1.24*10^{-7}$
7.00	$7.02*10^{-4}$	876.00	$1.19*10^{-7}$
10.00	$1.01*10^{-3}$	876.00	$1.14*10^{-6}$
15.00	$1.50*10^{-3}$	876.00	$1.09*10^{-6}$

Table 5. Four composite concentrations were synthesized, with final paraffin volumetric fraction concentrations of 21.8%, 40.3%, 50.1%, and 61.2%.

Conversion Chart	
Paraffin Concentration by Mass Percentage (%)	Volume Fraction (%)
3.00	21.83
7.00	40.32
10.00	50.15
15.00	61.17

Composite PCM Mixing Techniques

Various mixing techniques, particle size filtration investigations, and mixing apparatuses were considered to determine the optimal organic particle dispersion within the metallic PCM. Four techniques were investigated to create a procedure that was easily replicable, could scale with varying quantities of each composite, was inexpensive, and provided consistency between samples. These techniques ranged from a simple manual mixing process, a floating particle orientation study, the use of a non-contact planetary mixing centrifuge, and drop casting.

Manual Mixing

Manually mixing the two materials proved the most effective method to create the composite material. Figure 4 shows the simple mixing preparation and device set-up included a hot plate set to ~75°C, a wooden stirring rod, a mixing dish, and a scale to record the weight of the sample. A uniform, cubic-close packed solid structure was not obtained from this method. However, two supporting homogeneity studies and corrections in the computer simulations accounted for the disperse orientations of the paraffin particles embedded in the metallic substrate. In Figure 5, the three images show the transformation of the organic paraffin powder before and after the manual mixing to incorporate the Field's metal.

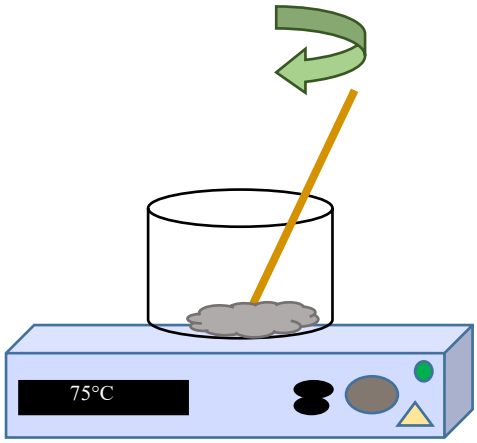

Figure 4. A schematic of the manual mixing process with a heat source below the mixing container holding the composite PCM sample.

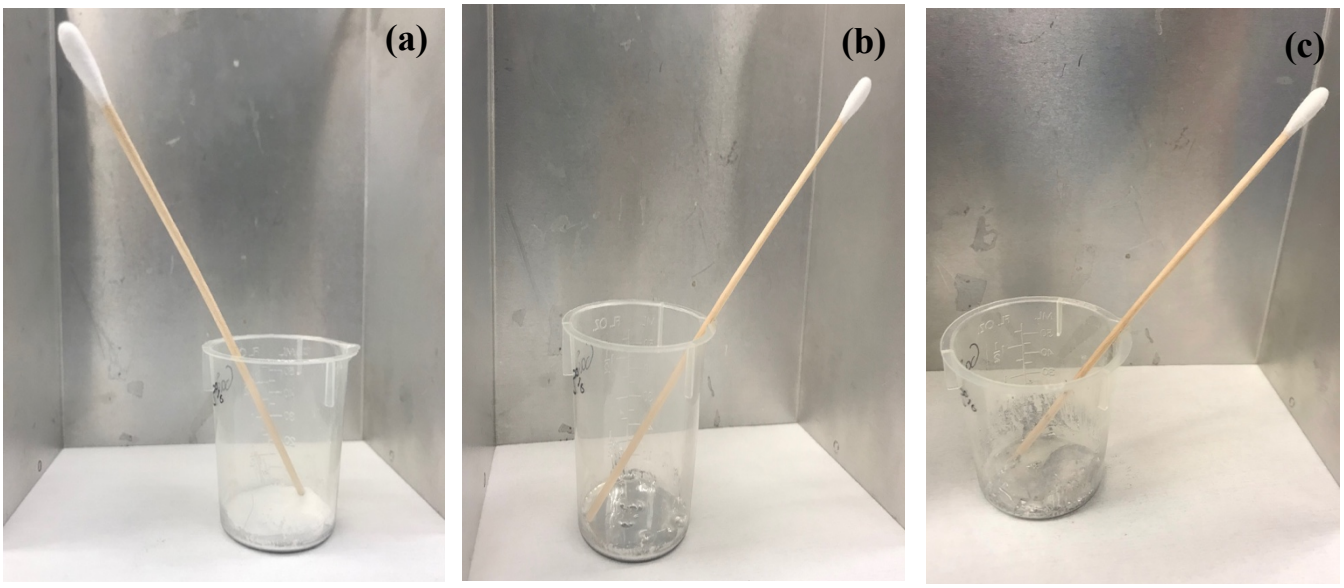

Figure 5. Beaker (a) contains paraffin dry powder compared to the Field's metal in (b). The 21.8% PCM composite after mixing is shown in (c).

Floating Particle Experiment

Another potential technique to align the spherical particles in a closely packed arrangement within the Field's metal was to conduct a floating particle experiment. This test would determine if the particles would float to the top of the liquified metal over time under elevated temperature conditions. Due to the lower density of the lighter organic PCM compared to the metallic PCM, we hypothesized that layers of aligned packed spheres would fit between the gaps of the adjacent particle layer. This orientation is shown in Figure 6.

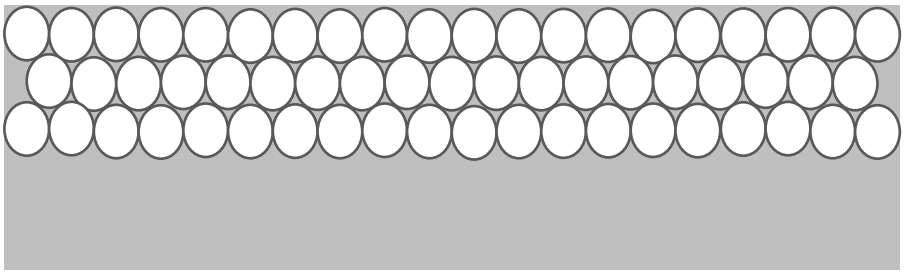

Figure 6. A simplified interior cross-section of paraffin particles floating to the top of the Field's metal substrate after mixing and solidification. Each subsequent layer is offset and Field's metal fills the interstitial spaces between the particles.

The two materials were initially manually mixed and left on the hot plate at 75°C for periods of 1 h, 3 h, 8 h, 24 h, and 72 h. After each time interval, the samples were left to solidify. The solid block was sliced in half, and both the interior and the top surface were observed under a microscope. Individual particles could be identified but they were dispersed and non-uniformly distributed. The particles did not form a floating particle structured layer, and some particles were observed at the bottom of the metal matrix. SEM and micro-CT videos also confirmed that complete segregation of the two materials did not occur.

While this experiment did not create the desired paraffin particle layer structure, it did confirm that, over many solid-liquid phase change cycles of the composite materials, the particles did not migrate or cluster in any specific area of the metal substrate. This finding is important, since these materials are intended to undergo numerous liquid-solid cycles within each eventual application. If the paraffin particles agglomerated, this would limit the composite PCM's ability to uniformly dissipate the input heat and efficiently store this thermal energy as latent heat within the material during the phase change.

Non-Contact Planetary Mixing Centrifuge Study

A Thinky ARE-250 mixing and degassing machine, which is a non-contact planetary mixture centrifuge, was another mixing apparatus explored within the study. The size and sample loading orientation are shown in Figure 7. This automated mixing process varied significantly from the manual mixing process. The dry powder was first packed into a syringe (21.8%), and then liquid Field's metal (78.2%) was added. Due to the poor wettability of Field's metal, the lowest powder-to-metal ratio was tested to provide the highest potential for mixing. In general, Field's metal does not easily maintain contact with other surfaces. The syringe was placed in an oven for 30 minutes at 125°C. While the packed syringe was in the oven, the mixing and degassing machine was adjusted for the syringe weight and the run time was set to 2 minutes.

After 30 minutes, the syringe was removed and immediately placed into the center receptacle of the non-contact planetary mixing centrifuge to minimize heat loss since there was not an interior heater. Once the run was completed and the sample was removed, a gray granular sediment was observed on the interior walls of the syringe and a liquid mass of Field's metal remained in the center. This process was repeated twice, but neither trial produced a homogeneous mixture.

Figure 7. The Thinky ARE-250 mixing and degassing machine.

Drop Casting

In drop casting, a solution is dispensed dropwise onto a substrate, where it typically spreads and forms a non-uniform thin solid film after solvent evaporation [2,7,33]. This technique initially seemed promising but was never tested due to unreliable uniformity within the coating and thickness. For accurate volumetric fractions of each material, the precision needs to be high. Another difficult complexity includes the bonding of the spheres together without infiltrating the voids. Ultimately, this method was rejected.

Final Technique Decision

Due to its simplicity and repeatability, manual mixing was chosen as the combination technique for the composite PCM samples. By increasing the amounts of paraffin particles, the composite PCM became more viscous, as can be seen in Figure 8d. The 61.2% volumetric fraction was chosen as the practical upper limit of the composite samples. The 21.8%, 40.3% and 50.1% experienced a similar physical phase change phenomenon from solid to liquid. The 61.2%

sample was a coarse solid, even under increased temperature conditions. The four liquid composites are shown in Figure 8.

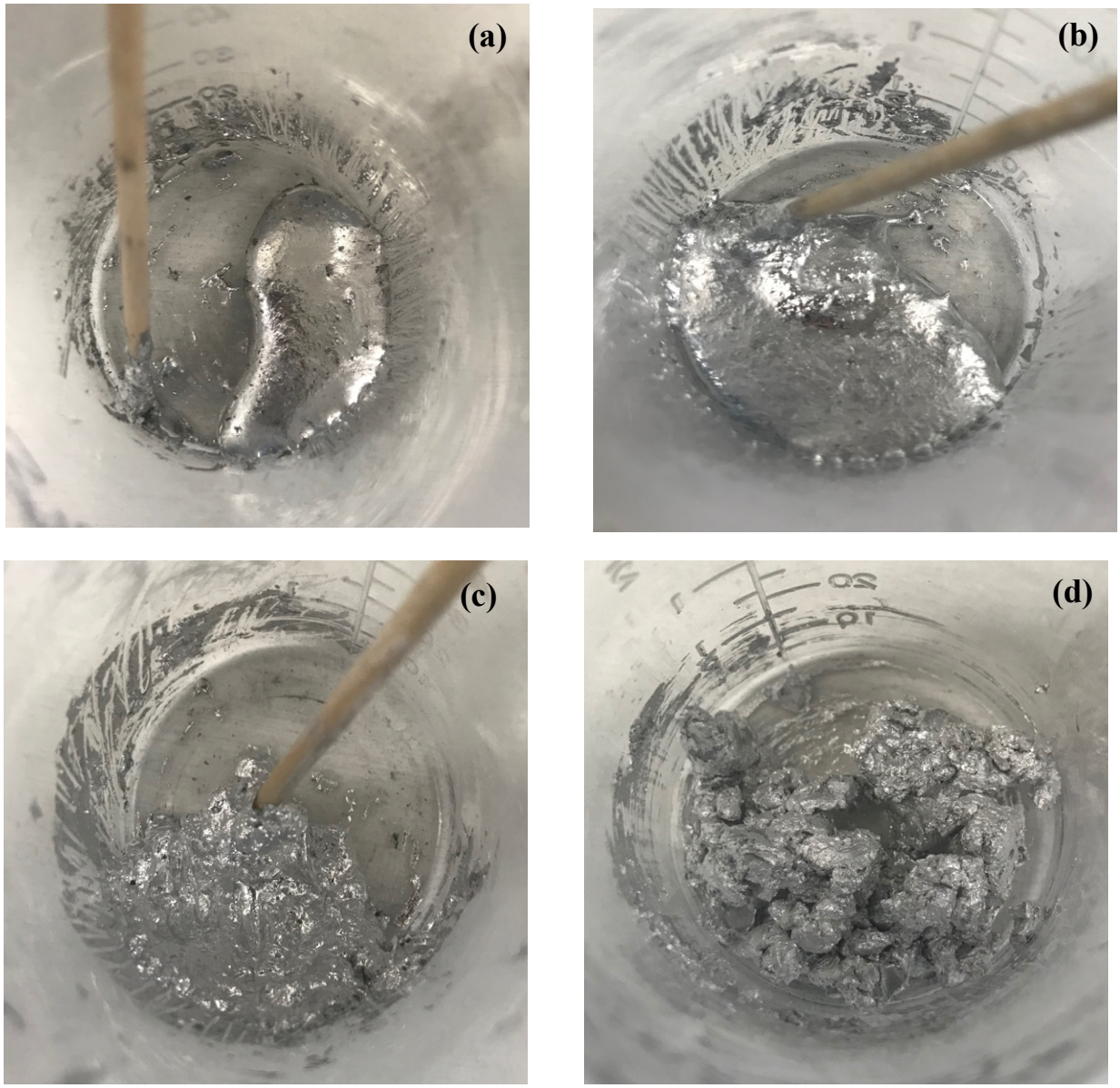

Figure 8. The four PCM composite samples are shown after manual mixing. In order from the upper left, the associated volumetric fraction concentrations are: 21.8% (a), 40.3% (b), 50.1% (c), and 61.2% (d).

Chapter 3: Mixture Homogeneity Study

Particle Dispersion Importance

Two methods were employed to determine the paraffin particle dispersion after the composite samples were fabricated and the powder had been successfully incorporated into the Field's metal. The chemical data sheet from Microtek Laboratories, Inc. provided minimal information on the physical characteristics or thermal properties of the paraffin powder. The product Nextek^{TM} 58D is a newly created synthesis of the low melting temperature paraffin products. Thus, thorough characterization studies of the material were required. In order to accurately model the phase change interactions of the materials and the temperature propagation through the composite, its topography and cross-section were both characterized.

Sample Preparations

To analyze the topography of each PCM composite sample, liquid samples of 4 mm^2 were left to solidify on a glass slide. Each solid composite sample was fastened with carbon black tape to a stage and inserted into the vacuum chamber of the Scanning Electron Microscope (SEM) for imaging. To ensure a flat surface was measured, the smooth underside of the sample was oriented upwards, towards the beam. Figure 9 shows four composite sample pieces before adhesion to the carbon black tape.

For powder imaging, a fine powder layer was deposited on one surface of a double-sided piece of carbon black tape. This tape was than attached to the SEM stage. The surface was lightly tapped to dislodge unadhered particles from the tape so they could not dislodge during charging by the electron bombardment during the imaging and focusing processes.

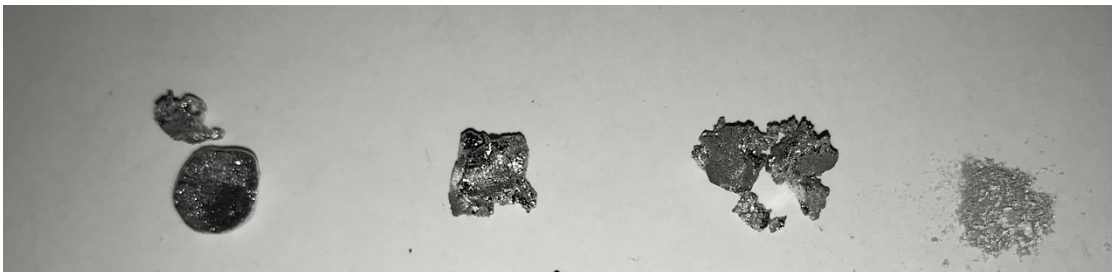

Figure 9. Four composite samples with paraffin concentrations of 21.8%, 40.3%, 50.1%, and 61.2%, from left to right. The 61.2% sample was almost granular due to the high concentration of paraffin.

Samples were simultaneously created for interior cross-section analysis with the micro-computed tomography system (micro-CT). Each of the four samples was melted and then molded into a triangular shape affixed to the top of a 2.5 in. long toothpick, as shown in Figure 10. The point of the composite cone provided a literal point of reference to accurately identify the sample within the micro-CT. The composite material adhered to itself and bonded with the wood, which prevented cracking or deterioration of the sample.

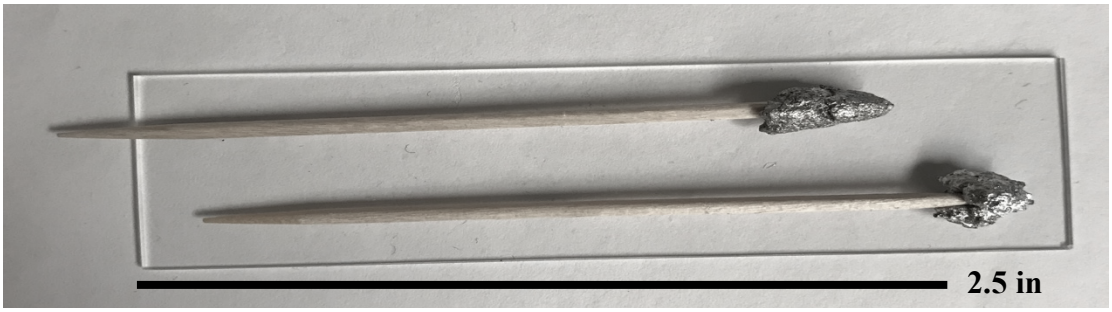

Figure 10. Two fabricated composite samples 21.83% (top) and 40.32 (bottom) affixed to toothpicks and are resting on a glass slide. Within the micro-CT testing chamber, each sample was positioned with the sample end of the toothpick uppermost and analyzed individually.

Scanning Electron Microscopy

A SEM produces images of a sample by scanning the surface with a focused beam of electrons. The electrons interact with atoms in the sample, producing various signals that contain information about the surface topography and composition of the sample. A Hitachi S4500 Field Emission Scanning Electron Microscope was used at various magnifications to obtain images of the PCM composite surface and the dry powder topology. A SEM has a condenser lens and objective lens. Each lens focuses the beam to a spot, rather than imaging the specimen. The voltage was set to 1.0 kV with magnitudes of either 5.00 K or 1.00 K, depending on the desired particle viewing window. Images of each sample were taken at scales of 300.0 μm, 60.0 μm, 30.0 μm, and 6.00 μm. The magnitude with corresponding length scales captured a randomly selected area of the sample as shown in Figure 11. Several images were taken at the same magnification to confirm the dispersion across the sample. The images exposed some Field's metal coating on the particles Figure 11 (2a-b). Ideally, all of the paraffin particles would be coated with Field's metal, but the images showed only partial coating for most particles.

Fully coated particles were desired because charging occurs to non-conductive specimens. To prevent charging of paraffin particles, operating conditions were adjusted for the incoming beam current to equal the sum of the outgoing secondary and backscattered electron currents. To meet this condition, all of the images were taken at a voltage of 5kV or below. When charging occurs, the particles appear shiny and begin to vibrate on the carbon black tape. If the beam current is large, the particles can dislodge from the tape and fly off into the vacuum chamber.

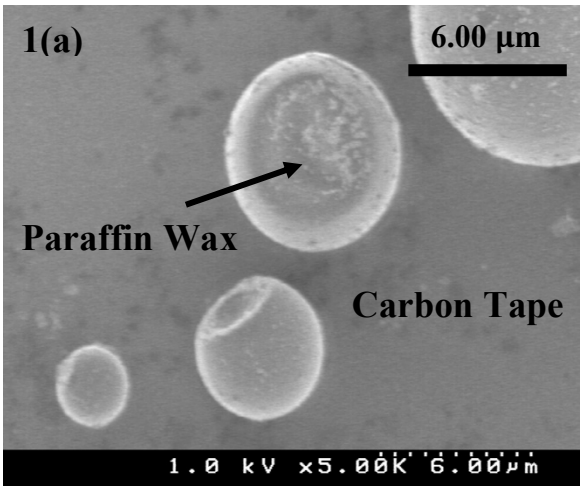
1(a)
6.00 µm
Paraffin Wax
Carbon Tape
1.0 kV x5.00K 6.00µm

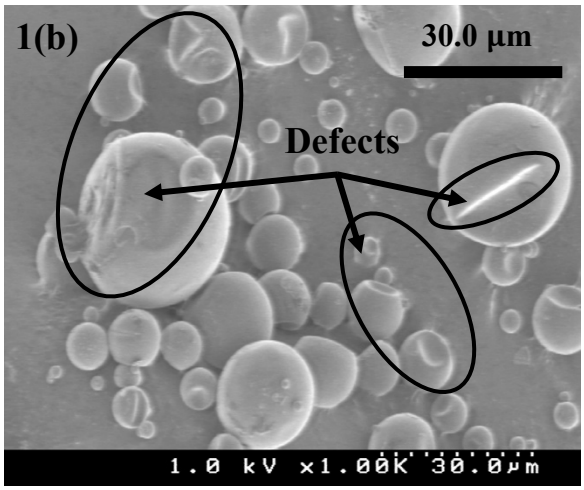
1(b)
30.0 µm
Defects
1.0 kV x1.00K 30.0µm

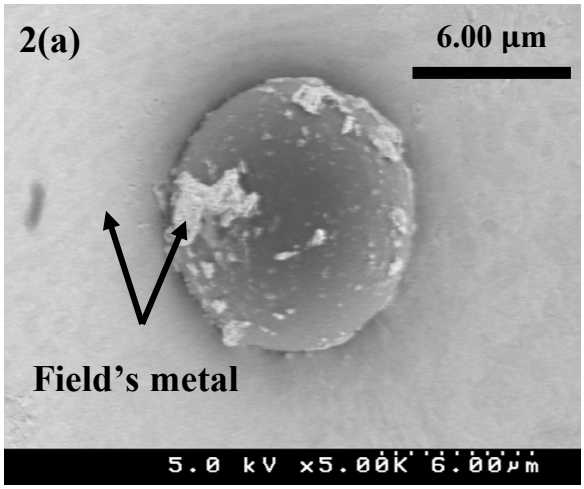
2(a)
6.00 µm
Field's metal
5.0 kV x5.00K 6.00µm

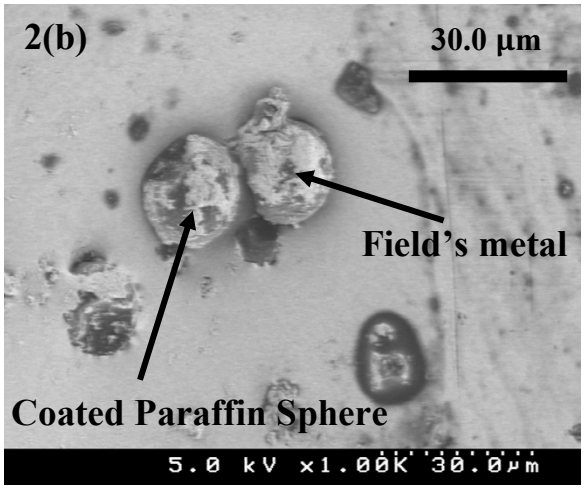
2(b)
30.0 µm
Field's metal
Coated Paraffin Sphere
5.0 kV x1.00K 30.0µm

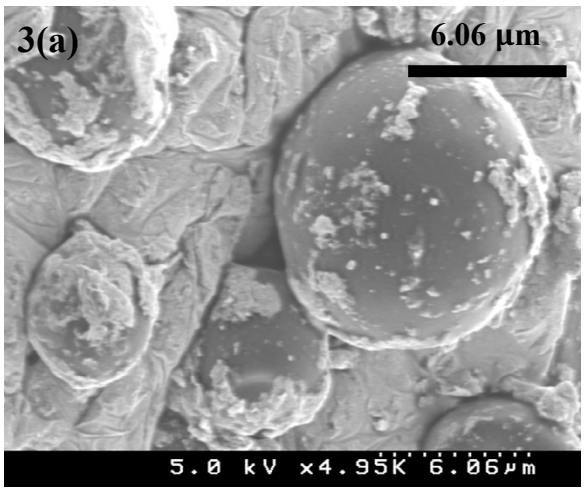
3(a)
6.06 µm
5.0 kV x4.95K 6.06µm

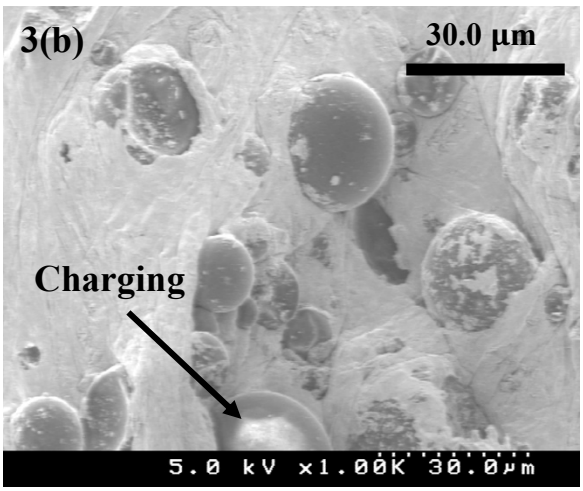
3(b)
30.0 µm
Charging
5.0 kV x1.00K 30.0µm

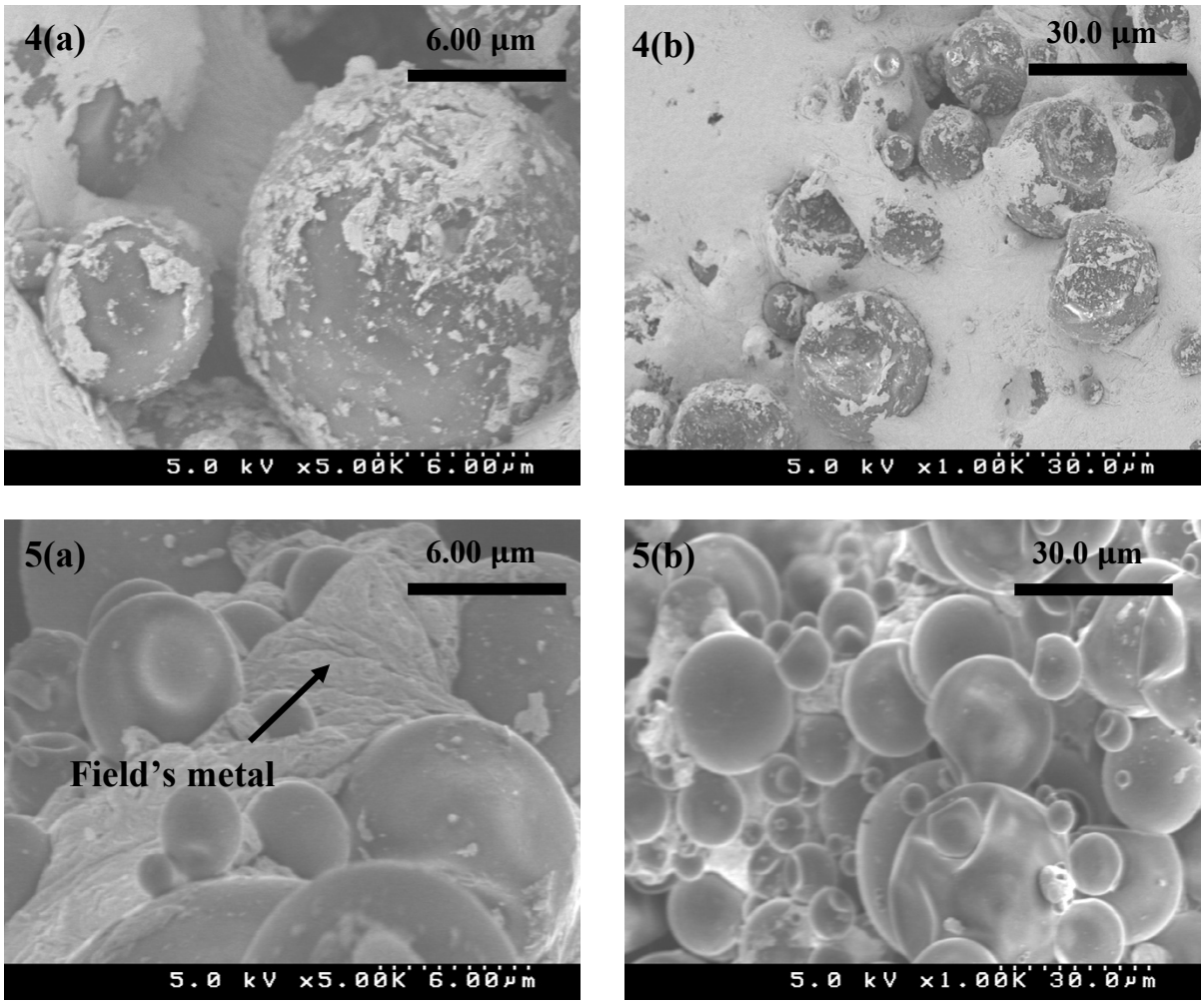

Figure 11. SEM images of each PCM composite sample: 100.0% (1), 21.8% (2), 40.3% (3), 50.1% (4), and 61.2% (5) paraffin wax volumetric concentrations. Each sample concentration corresponds to the images horizontally. For example, the top left and right images in 1 (a-b) correspond to 100.0% or pure paraffin at 6.00 µm and 30.0 µm. The reference scale bar for particle sizing is located at the bottom right corner of each image as a dotted line.

In addition to fully and partially coated particles, the images show some particles partially embedded in the Field's metal as in Figure 11 3b. However, the particle size distribution

varied widely in comparison to the vendor's given size of approximately 15-30 μm. Particles as small as 1.5 μm and as large as 44 μm were measured. Deformation of particles was also observed in the solely dry powder form, indicating that particle deflation had occurred before any manual mixing as shown in Figure 11 1a-b. The variable size distribution and particle shape distortion across each sample were unanticipated results from the SEM topology analysis. The asymmetry of the particles could not be conveyed in the computer modeling, but this phenomenon can be assessed in the error analysis.

Micro-Computed Tomography Videos

Techniques to physically slice the composite samples were initially attempted to analyze the material's cross-section. However, Field's metal does not symmetrically break across natural planes of separation. A brittle material, it tends to crumble under pressure. If the material breaks around the paraffin particles, leaving voids, then the measured cross-sectional areas would be inconsistent from sample to sample. Thus, a non-destructive manner to examine the interior of the samples was sought.

Micro-CT provided 3D images of the internal structure of the PCM composite samples without damage. A computer-processed compilation of many X-ray measurements were taken from different angles to produce tomographic images of a specific area of the scanned composite. With a ZEISS Xradia 510 Versa 3D X-ray Tomography System, time-lapse videos were taken of each composite concentration affixed to a toothpick. Each individual skewer sample consisted of a molded tip-like arrowhead of 50.1%, 40.3%, and 21.8% volumetric concentration of paraffin. Due to the granular physical characteristics of the 61.2% composite, the sample was inserted into a plastic tube affixed to a toothpick. Both ends of the tube were plugged with epoxy.

The internal distribution of the particles inside of the metal substrates were clearly displayed after 72-hour scans at high resolution as shown in Figure 12b. Each sample was also scanned at a low resolution, but these videos were disregarded in the postprocessing analysis because they lacked adequate color separation and image quality for the binarization assignment conversion to a gray scale as shown in Figure 12a. Two resolutions were run for comparison and to show the cross-sectional slices of the PCM composites at different magnifications. A video resolution comparison between each PCM composite is shown in Appendix C in Figures 30-33.

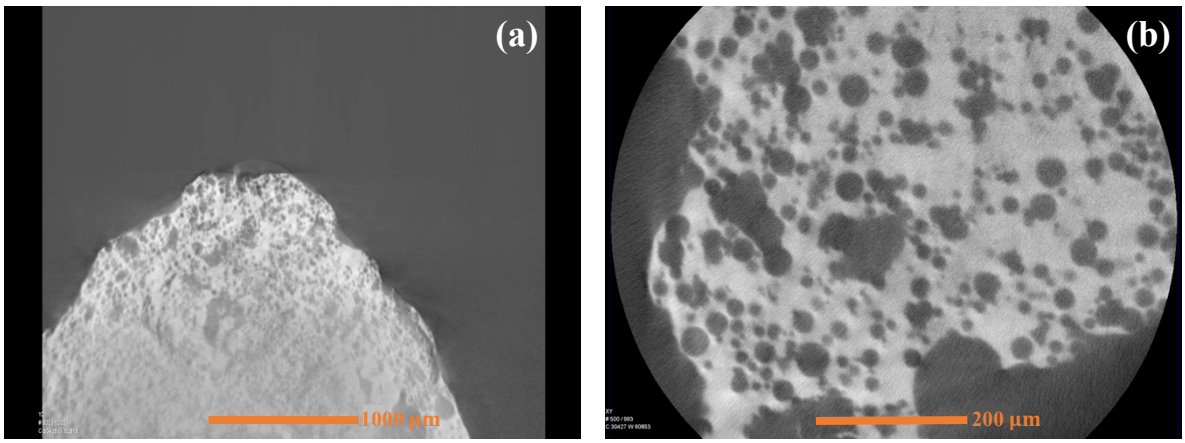

Figure 12. Both images consist of the same 40.3% composite run at different resolutions at frame 500. The left image (a) shows the lower resolution with a scale bar of 1000 μm. With definitive particle color separation in comparison to the lighter metallic substrate, the right high-resolution image (b) has a scale bar of 200 μm. This clarity trend associated with the high-resolution scan was consistent for the other three composite compositions.

In order to determine the exact sphere distribution, still images were taken from the time-lapse videos created by the micro-CT. These images were converted from a RGB to a gray scale in MATLAB as shown in Appendix D. The threshold technique employed was BW = imbinarize(I), which creates a binary image from a 2D or 3D grayscale image by replacing all

values above a globally determined threshold with a value of 1. All remaining values were set to 0s. The Imbinarize technique traditionally uses Otsu's method, which chooses the threshold value to minimize the intraclass variance of the thresholded black and white pixels[22]. Imbinarize uses a 256-bin image histogram to compute Otsu's threshold. The images of manually calculated mass converted volume fractions of 61.2% 50.1%, 40.3%, and 21.8% were analyzed. Still images were compiled, and the particle concentrations were averaged within the specified area. Each video was then overlaid with a grid, which correspond to the MATLAB coordinates. Each specified area was shifted in in relation to the x-axis or y-axis. The x-axis corresponded to a left or right movement by scaling the width of the threshold box. The y-axis scaled with the box height from top to bottom. Figure 13 shows an example of the grid structure. The number of frames averaged depended upon the quality of the video duration and before the transition into blackness occurred. After each sample area was chosen during the micro-CT and the MATLAB code was run, an averaged, pixelated image was also formed as shown in Figure 14.

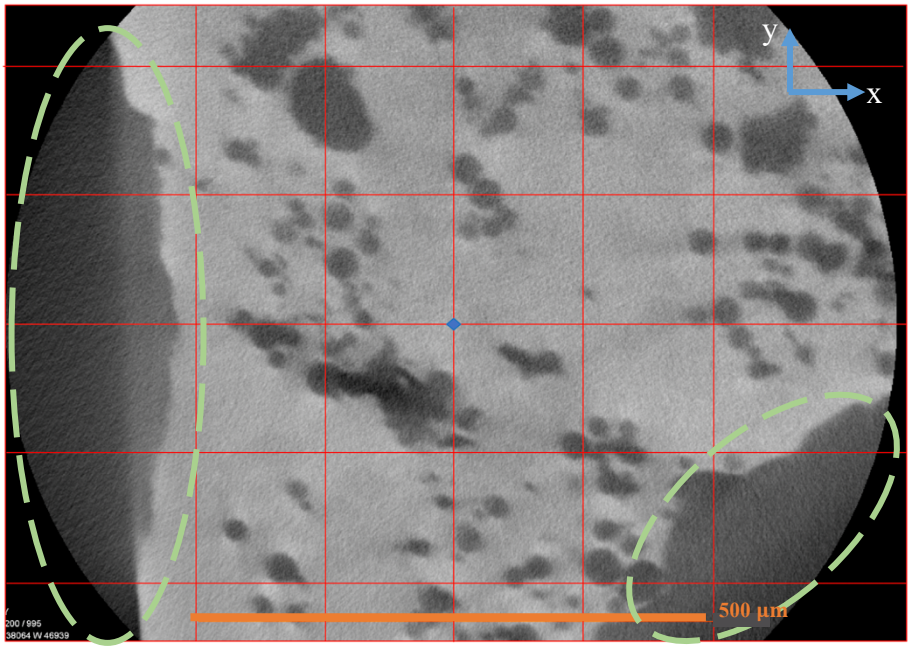

Figure 13. The 21.8% PCM composite showing the grid structure based on the orange 500 µm scale bar. The blue diamond indicates the center of the image. The green dashed ovals outline the beginning of the fade to black since the material has been sliced over halfway through with x-rays. These faded regions were ignored for the particle dispersion calculation since they are not part of the sample.

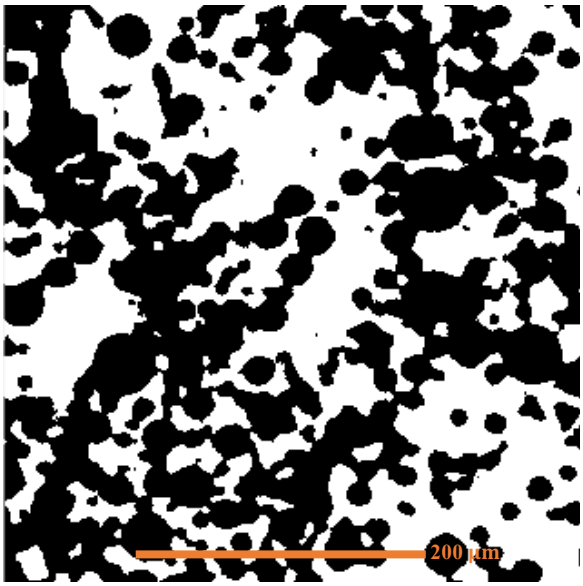

Figure 14. This binarized image depicts the average cross section particle (black) dispersion throughout the Field's metal (white) over 450 frames of the 40.3% paraffin volumetric fraction composite.

Table 6 relates the composite PCM volume fraction values derived from the mass conversions and the MATLAB script paraffin volume fractions. The standard error relates to the precision of estimation which was calculated from the sample mean ($\overline{X}$). This was set as a point of the population mean (µ). The standard error of $\overline{X}$ measures how precisely $\overline{X}$ estimates µ. In a normal distribution with mean µ and variance σ^2, the standard error of $\overline{X}$ is:

$$\sigma_{\overline{X}} = \frac{\sigma}{\sqrt{n}}.$$

However, in this calculation, σ is unknown so the sample standard deviation (S) is substituted into the above equation. The estimated standard error of $\overline{X}$ related to the particle distribution was calculated from the equation:

$$\hat{\sigma}_{\overline{X}} = \frac{S}{\sqrt{n}}.$$

Table 6. The relationship between the calculated mass to volumetric fraction and the average micro-CT volume fraction analysis are shown. The difference column refers to the variation between the mass to volume fraction conversion column and the average micro-CT volume fraction column. Both the standard deviation and standard error were calculated over 5 regions of the micro-CT videos.

PCM Composite Particle Volume Fraction Comparaison				
Mass to Volume Fraction Conversion	Average Micro-CT Volume Fraction	Difference	Micro-CT Standard Deviation	Micro-CT Standard Error
21.8%	25.8%	4.0%	±1.26%	±0.56%
40.3%	44.5%	4.2%	±2.18%	±0.97%
50.1%	55.1%	5.0%	±1.47%	±0.66%
61.2%	64.2%	3.0%	±8.84%	±3.95%

The PCM composite 61.2% sample had the closest value compared to the micro-CT volumetric fraction (64.2%). In general, the four micro-CT volumetric fraction calculations followed the same trend as the mass converted samples with the more paraffin particles yielding higher concentration values. A complete summary of each sample location and sample standard error can be found in Appendix E. These values ranged from 3.0% to 5.0% departure from the mass calculations.

Discrepancy between the values could have resulted from the poor wettability of the two materials. The sample was granular at the upper limit of 61.2% paraffin volumetric concentration. This was not consistent with the other three PCM composites, which had definitive liquid regimes under a heat flux. The 21.8% sample had the most consistent volumetric fraction values at each sample location. The increase in paraffin particles showed relatively higher volumetric fractions with the use of micro-CT analysis in comparison to the mass converted values. Despite the deviation in the volumetric fraction comparison within the PCM composites, all samples showed particle dispersion throughout the sample.

When comparing the mean derived from the micro-CT still images to the mass calculated volumetric fractions, all variations were below 5.0%, which supported the cross-sectional averaged areas to the anticipated volumetric fraction values.

Topography and Tomography

Due to the limited commercial characterization of the paraffin particles, this study analyzed the dispersion of the melamine coated particles within the Field's metal. This inquiry was prompted from the SEM images exposing morphologies in the particle shapes and nonuniform metallic particle coatings post mixing. In order to accurately model the heat dispersion through the composite and confirm the accuracy of the conversion of mass to volumetric fraction calculation, an interior cross-sectional analysis was required. The micro-CT x-ray imaging technique permitted a non-destructive view into the interior of the composite samples. The topography of the metallic coating over the particles was shown in the SEM images, but the tomography from the micro-CT confirmed the study's initial hypothesis of particle dispersion throughout the composite material.

Chapter 4: Thermal Properties- Measurement and Material Characterization

PCM Thermal Properties

The thermal material properties were not provided on the data sheet by the vendor for the organic PCM particles. Thus, to adequately quantify each PCM composite's thermal properties, the latent heat of fusion, peak melting temperature, phase change onset, and thermal conductivity of each sample is measured. The latent heat of fusion measures the energy absorbed or released by a substance to change the physical state (solid, liquid, or gas) without changing the material's temperature. Latent heat is expressed as the amount of heat (joules) per unit mass (g) of the substance undergoing a phase change. In this study, the phase change onset is described as being the beginning transition (melting or solidification) between the solid and liquid states due to a temperature input into the system. The peak melting temperature (°C) is defined as the melting point where the material has the highest temperature after a phase transformation from solid to liquid occurs. These three thermal parameters were measured with a differential scanning calorimeter (DSC). The fourth parameter is thermal conductivity (W/mK), which measures a material's ability to transmit heat. Thermal conductivity was characterized by time-domain thermoreflectance (TDTR) at the Army Research Laboratory. The TDTR endeavor was led by Dr. Adam Wilson. For this chapter, the DSC measurements will be presented first and then the TDTR measurements will follow. A discussion of each technique will accompany the calculations.

Differential Scanning Calorimetry

The PCM composite mixtures were characterized with the aid of the thermoanalytical technique: DSC. This machine heats two materials, a sample and a reference, at a constant, specified rate. The calorimeter records the time-dependent temperature of each material using a

thermocouple. The sample material can also be compared relative to an empty reference pan. The two materials' heat capacities are different, thus the rate at which they heat, and the corresponding temperatures will also be dissimilar. This difference is innate to the materials themselves[16].

Each sample was weighed in an aluminum sample pan and placed into a Perkin Elmer DSC 8500. For accurate measurements, each material was heated on a hot plate and spread across the bottom surface of the pan, as shown in Figure 15.

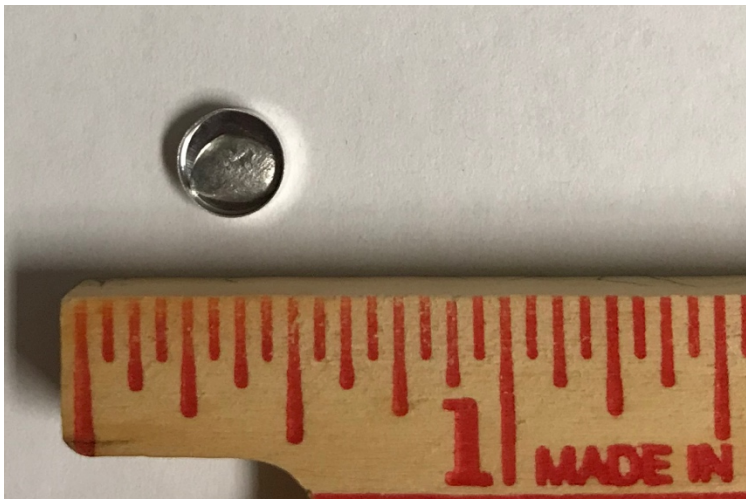

Figure 15. A pure Field's metal sample in an aluminum DSC pan. Due to the DSC's weight (< 200 mg) and Field's metal's poor wetting properties, the entire bottom surface was not uniformly covered.

For each PCM composite, pure Field's metal, and pure microencapsulated paraffin wax sample, three cycles were run starting at 25°C, with an increasing ramp rate of 0.5°C/min until 85°C was reached. The temperature was then held constant for 5 minutes at 85°C. A decreasing ramp rate of 0.5 °C/min followed until a temperature of 40°C was yielded. This cycle was then repeated twice more for a total run time of approximately 13 hours. A chiller was connected to

the DSC to aid in the ramp down process, however, subambient temperatures were not necessary for this project. Figure 16 is a description of the heat flow curves from the DSC. The heat flow changes as energy is added or removed from the system. An endothermic process occurs whenever heat is added from a system to melt a sample. As the sample begins to solidify, heat is released to the environment, thus yielding an exothermic process.

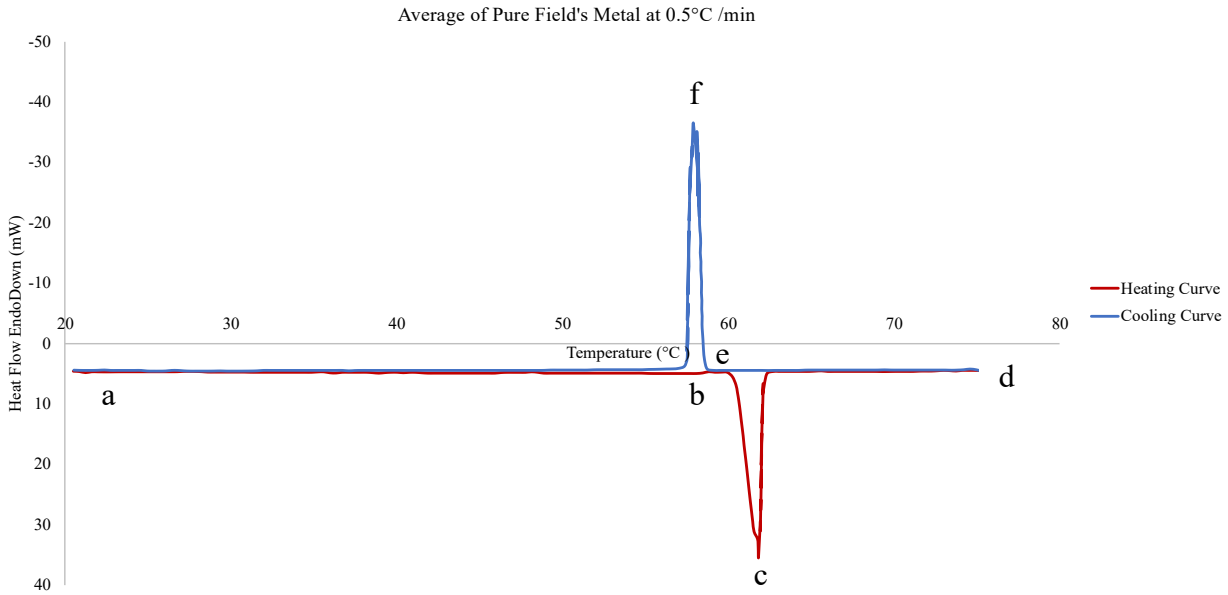

Figure 16. Key features of a DSC graph sample include the: (a) cycle starting point, (b) start of the endothermic phase transition (melting), (c) peak energy of endothermic phase transition, (d) isothermal regime, (e) start of exothermic phase transition (solidification), and (f) peak of exothermic reaction. The heating curve is colored red and the cooling curve is blue. This pure Field's metal graph represents the typical shape of a DSC curve.

Initially, the ramp rate was set to 5°C/min with endpoints at 40°C and 95°C. However, with the composite samples, this led to a curve shadowing effect. As shown in Figure 17, the pure

Field's metal and the pure paraffin heat flow curves are overlaid. The complete area of the paraffin melting curve cannot be identified. To determine the latent heat of each constituent material in the composite, the mass-weighted area under the respective curves must be able to be measured. Figure 17 and Figure 18 show the overlaid curves and the 40.3% paraffin composite for reference. The lower ramp rate of 0.5°C/min was chosen to broaden and sharpen the distance between the peaks.

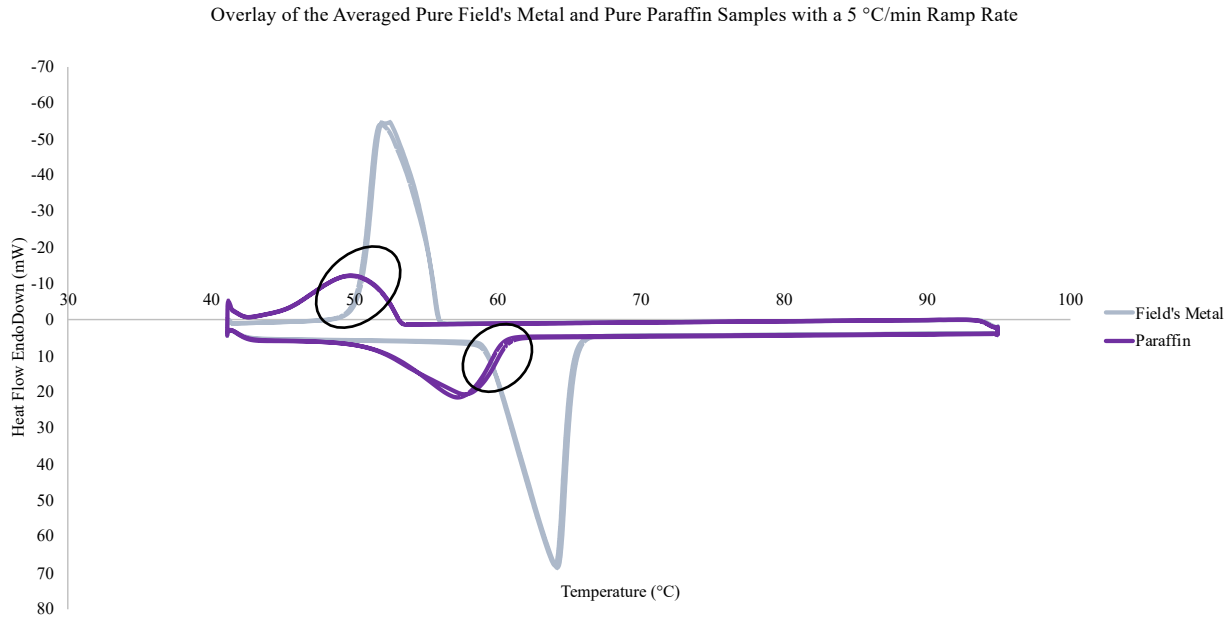

Figure 17. The heat flow of the individual pure organic (purple) and metallic (gray) PCM samples. The black ovals indicate the areas of overlap under a ramp rate of 5°C/min.

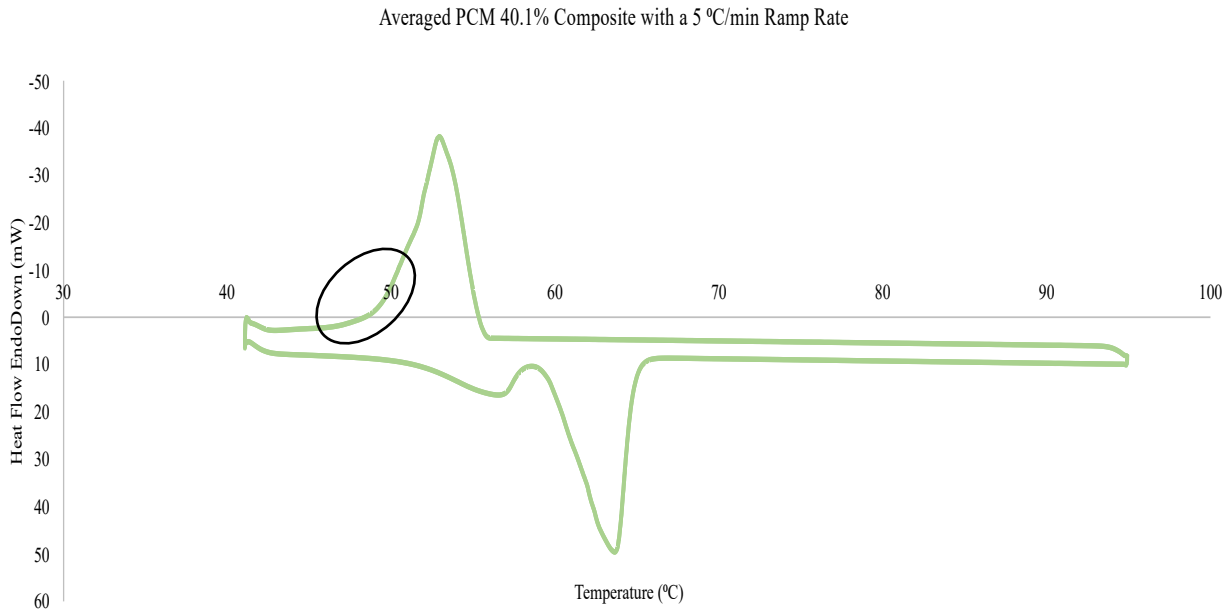

Figure 18. The heat flow of the 40.1% composite showing that the organic PCM solidification curve is subsumed by the solidification curve of the metallic PCM. This is depicted by the black oval.

With the lowered ramp rate of 0.5°C/min, the peak area of each the paraffin wax and Field's metal curves could be sufficiently measured using the Pyris Series-DSC 8500 software tool. The latent heat of each PCM composite sample was calculated by determining the mass-weighted area under the curve. This refers to the auto-computed DSC value for the latent heat. The equation used for a single constituent sample is:

$L_1 = (AUC_1 / \text{Total Sample Mass})$,

where L_1 represents the calculated latent heat (J/g), the term (AUC) is the software output mass-weighted area under the curve (J), and the total sample mass is measured in grams.

For a sample with two constituents, the equation is:

$L_1 = (AUC_1/Mass_{tot})/(Mass_1/Mass_{tot}) = (AUC_1/Mass_{tot})/\%$ weight.

This equation was used for the PCM composite systems. These calculations are shown in Table 7 and Table 8.

Table 7. The mass of the constituent materials in the PCM composites is shown.

Sample Mass Constituent Calculations			
Sample	Mass (g)	Microencapsulated Paraffin (g)	Field's Metal (g)
21.8%	0.123	0.00370	0.120
40.3%	0.0618	0.00433	0.0575
50.1%	0.0401	0.00401	0.0361
61.2%	0.0379	0.00568	0.0322
Pure Field's Metal	0.125	-	-
Pure Microencapsulated Paraffin	0.0629	-	-

Table 8. The latent heat of the individual constituents of each composite sample is shown. Pure Field's Metal had a latent heat value of 49.9 J/g. The DSC graphs for pure Paraffin were inconclusive.

Latent Heat (J/g)									
21.8% Composite		40.3% Composite		50.1% Composite		61.2% Composite		Pure FM	Pure Paraffin
FM	Paraffin	FM	Paraffin	FM	Paraffin	FM	Paraffin	-	-
46.6	323.1	47.4	219.6	44.6	289.4	46.6	176.9	49.9	-

In literature, the latent heat obtained from DSC heating runs is 25.4 J/g for Field's metal[27]. Hassan et al. (2016) identifies pure paraffin wax having a latent heat up to 259 J/g. For an

encapsulated paraffin in urea-formaldehyde comparison, the latent heat of fusion is between 102-204 J/g[12]. Urea-formaldehyde is a thermosetting polymer. The latent heat calculated in Table 8 for both the pure FM and PCM composite systems is much higher than the literature values. The inconsistency in the measured data compared to literature values could be the result of consistent underestimation of the sample mass. However, a microbalance was used to weigh the samples. Another more realistic factor could be calibration inconsistencies within the DSC. The DSC graphs showed peak degradation and misalignment of the isothermal area. For consistency, the samples should be run in a second DSC for comparison.

Next, the onset of melting was calculated. This occurs at the point where the tangent of the inflection point intersects the base of the curve. The beginning melting temperature or phase onset point can be identified by the DSC heat flow curve. Within the analysis software, a tie line was drawn from the beginning of the reaction, across the horizontal valley, to the end of the reaction. From here, another line was drawn from the curve of interest's inflection point until it intersects with the tie line. The point where the lines intersect is the eutectic or organic PCM melting temperature[18]. Within this study, only the melting curve's onset and peak temperature were recorded. Table 9 and Table 10 display these values. The average melting onset temperature is 58.2°C for Field's metal. The average onset temperature for the microencapsulated paraffin is 48.2°C. Both of these values are within 0.1°C across all five samples. The average peak temperature for the Field's metal melting curves is 61.3°C, while the average temperature for the organic PCM is 55.9°C. Figure 19 (a-e) shows the physical DSC curves over three cycles for each sample. The expected melting temperatures were 58.0°C and 59.0°C for the respective organic and metallic PCM constituents based on the data sheets from each vendor.

Table 9. The onset phase change temperatures within the heating curve of the DSC graph over three cycles.

Average Melting Onset Temperature (°C)								
21.8% Composite		40.3% Composite		50.1% Composite		61.2% Composite		Pure FM
FM	Paraffin	FM	Paraffin	FM	Paraffin	FM	Paraffin	-
58.1	48.2	58.2	48.3	58.1	48.2	58.2	48.2	58.2

Table 10. The peak temperature within the heating curve of the DSC graph over three cycles.

Average Heating Peak Temperature (°C)								
21.8% Composite		40.3% Composite		50.1% Composite		61.2% Composite		Pure FM
FM	Paraffin	FM	Paraffin	FM	Paraffin	FM	Paraffin	-
61.2	55.8	60.8	55.7	61.6	56.0	61.6	56.0	61.1

(a)

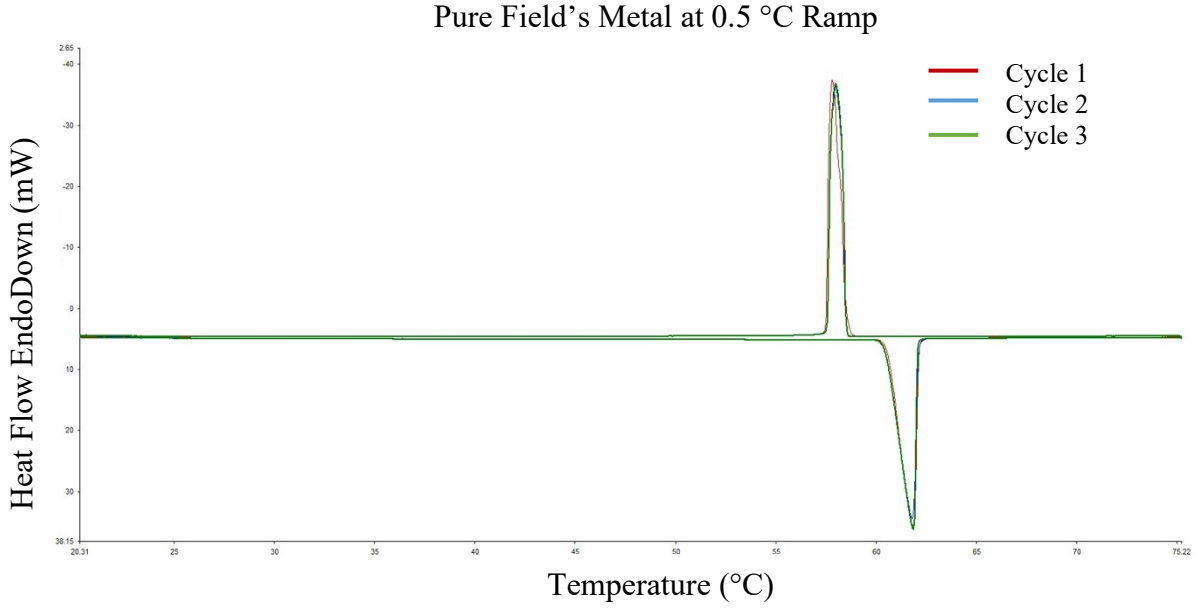

(b)

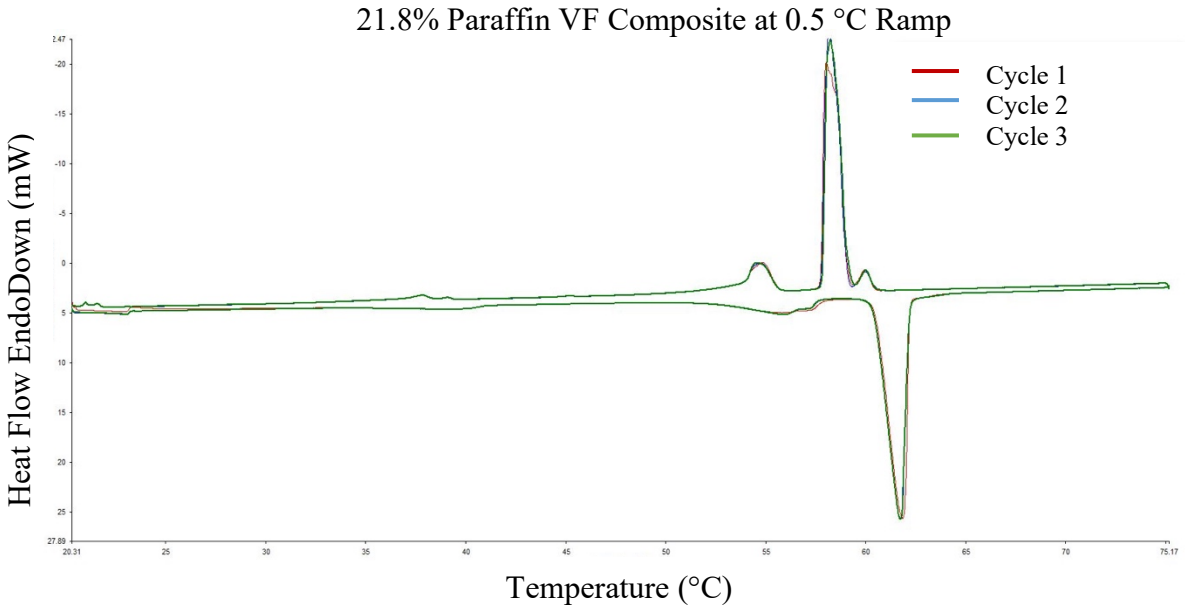
21.8% Paraffin VF Composite at 0.5 °C Ramp
Cycle 1
Cycle 2
Cycle 3
Heat Flow EndoDown (mW)
Temperature (°C)

(c)

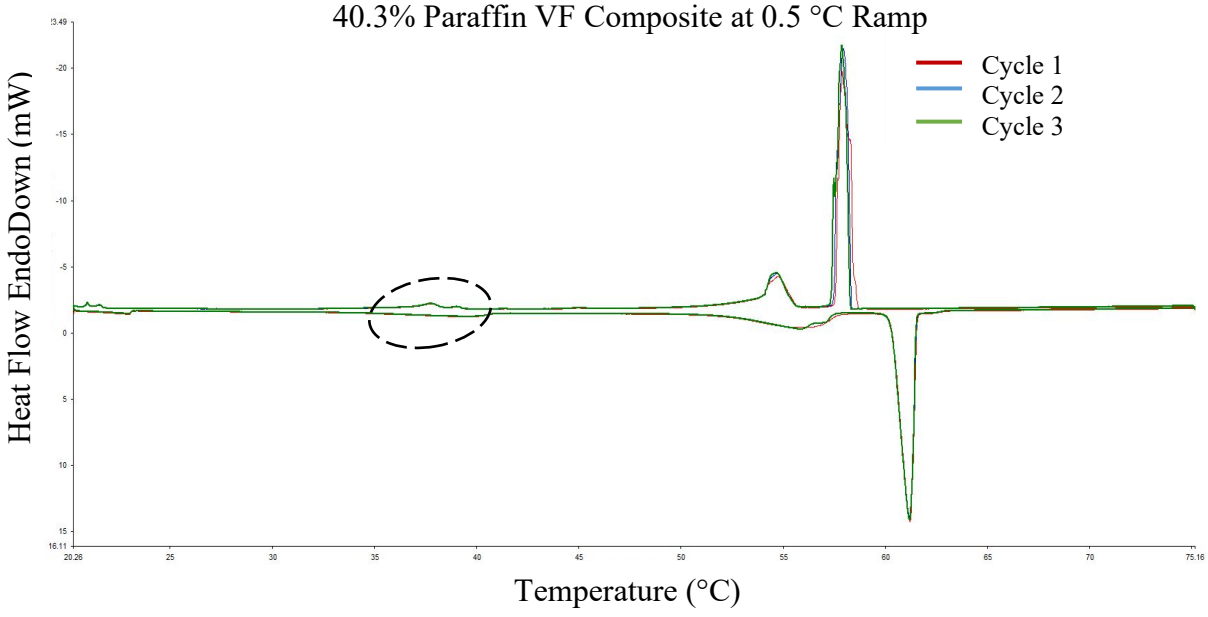
40.3% Paraffin VF Composite at 0.5 °C Ramp
Cycle 1
Cycle 2
Cycle 3
Heat Flow EndoDown (mW)
Temperature (°C)

(d)

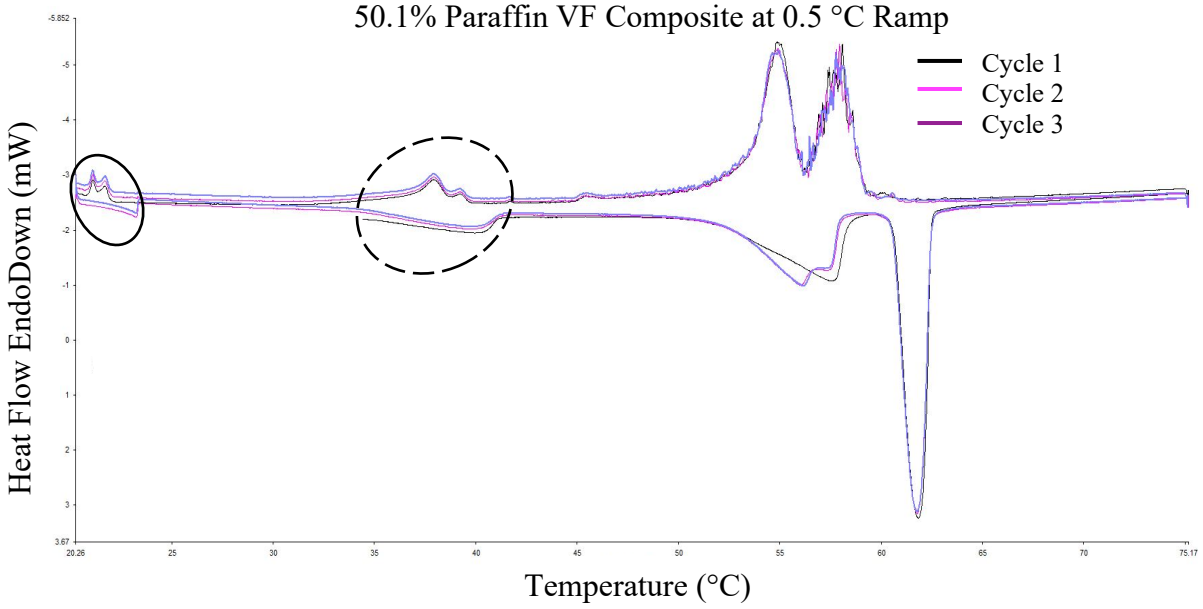
50.1% Paraffin VF Composite at 0.5 °C Ramp
Cycle 1
Cycle 2
Cycle 3
Heat Flow EndoDown (mW)
Temperature (°C)

(e)

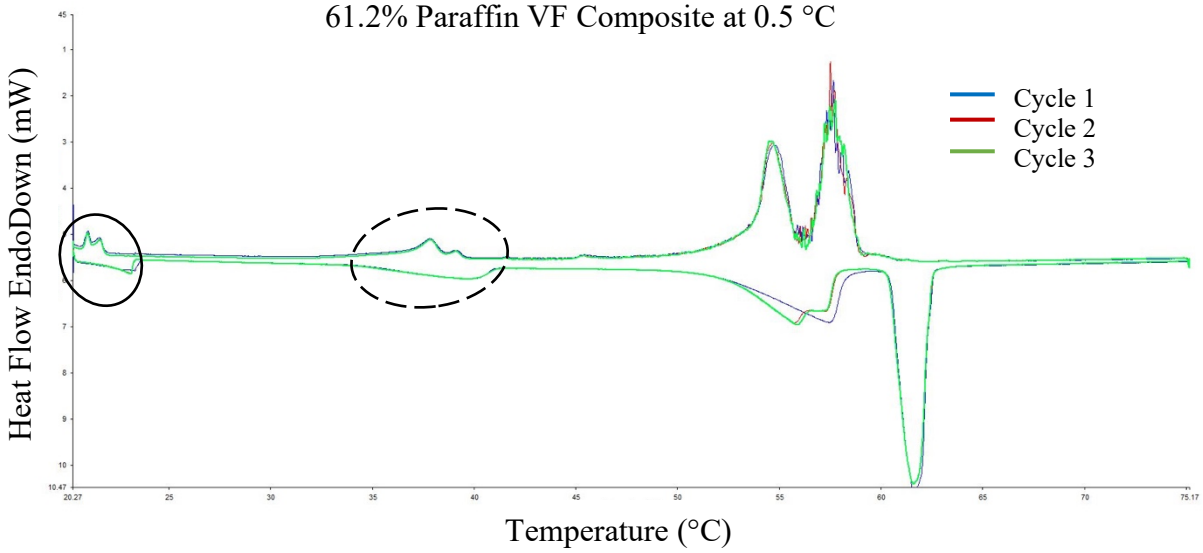
61.2% Paraffin VF Composite at 0.5 °C
Cycle 1
Cycle 2
Cycle 3
Heat Flow EndoDown (mW)
Temperature (°C)

Figure 19. The pure Field's metal and the four PCM composite DSC curves are shown (a-e). As the concentration of the organic PCM increased, the curves became more deformed. The black solid circle in (d) and (e) show artifacts within the graph. The dashed oval (c-e) indicate a double valley, which suggests a transition period where the reaction does not emit or absorb a linear amount of energy, but rather, a smaller initial release/absorption of energy and then a larger secondary event[18].

A usable DSC curve for the pure organic PCM could not be obtained for the 0.5°C/min ramp rate. Despite the deformation in shape with the higher concentration of microencapsulated paraffin wax, the phase onset temperature and peak melting temperature remained consistent across the five samples. From the DSC analysis, the latent heat was also found for each sample. Further testing in regard to a reference sample instead of an empty pan would be necessary to measure the specific heat of the system. Future studies are encouraged to investigate this parameter.

Time-Domain Thermal Reflectance (TDTR)

TDTR is a versatile and powerful technique for thermal characterization, which leverages temperature-dependent changes in surface reflectivity to interpret thermal properties. TDTR has been used to study both solids[23,25,28,30,31] and liquids[24, 29]. This testing apparatus demonstrates sensitivity over a wide range of sample thermal conductivities.

The thermal conductivity was investigated on a selected subset of the composite samples, which are representative of the range of expected values. To test the accuracy of the device, a pure Field's metal sample was included for comparison with existing literature values. The pure Field's metal sample was expected to have the highest thermal conductivity, which has been

reported to be 17.7 W/m K near room temperature[19]. The two tested PCM composite samples were the 21.8% and 40.3% organic concentrations, which were expected to have lower values owing to paraffin wax's low thermal conductivity[25]. The 50.1% and 61.2% composites were not tested due to the higher density of paraffin spheres. The TDTR laser must be able to probe through the sample without measuring a complete field of organic spheres.

For the three samples, a physical holder was required to confine the sample during both the solid and liquid phases. Figure 20 depicts the concept of sandwiching the sample between two 3-inch glass microscope slides. While the sample was in a liquid state, it was deposited onto a glass slide with an approximate 80 nm of evaporated aluminum base layer. The slide was resting flush against a laboratory benchtop with the aluminum facing upward. Then, the top layer of glass was placed. Once solidified, the interstitial space between the glass was filled with epoxy to create a seal.

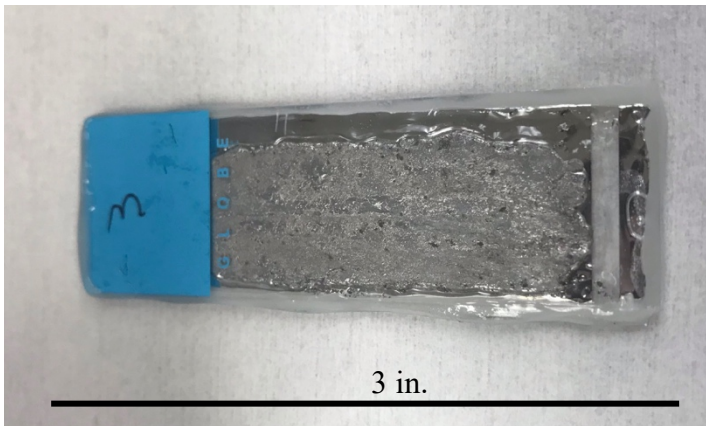

Figure 20. The sample structure for the TDTR testing containing the 21.8% PCM composite with clear epoxy surrounding the exterior edges.

Personal Discussion with Dr. Adam Wilson

The TDTR system setup was led by researchers at the Army Research Laboratory. In general, TDTR leverages a femtosecond pulsed laser to simultaneously heat the sample and monitor the time-dependent temperature decay via temperature-dependent changes in surface reflectivity. The implementation of TDTR controls an optical parameter oscillator (OPO), which converts the incoming 80 fs pulsed laser source at 820 nm into a 410 nm source. This is used as the pump and the remaining 820 nm source is used as the probe. The pump is then sent through an electro-optic modulator, which modulates the pump beam to a sine wave envelope. This is then directed to the sample. The probe beam is sent to a delay stage, which adjusts the probe path length, thereby changing the timing of the arrival of the probe beam with respect to the pump. By increasing the path length, the probe arrives after the pump at a time related to the change in path length times the speed of light. The reflected probe is then collected at a photodetector, and the signal is sent to a lock-in amplifier, which is locked into the pump's modulation frequency. By collecting data at several values of delay time, the absorption of the pump and subsequent thermal dissipation was recorded and fit to a multi-layer heat transfer model[6,23]. TDTR data is typically reported either as the offset in phase between the pump modulation and the measured probe signal, or the ratio of the in-phase and out-of-phase components of the signal. In this work, the ratio is reported as the raw data to measure thermal conductivity. The advantage of using phase and/or ratio as opposed to magnitude is that these quantities are much less susceptible to fluctuations in laser power and provides a generally cleaner signal to work from for fits of the data. Figure 21a depicts the experimental schematic used in this study.

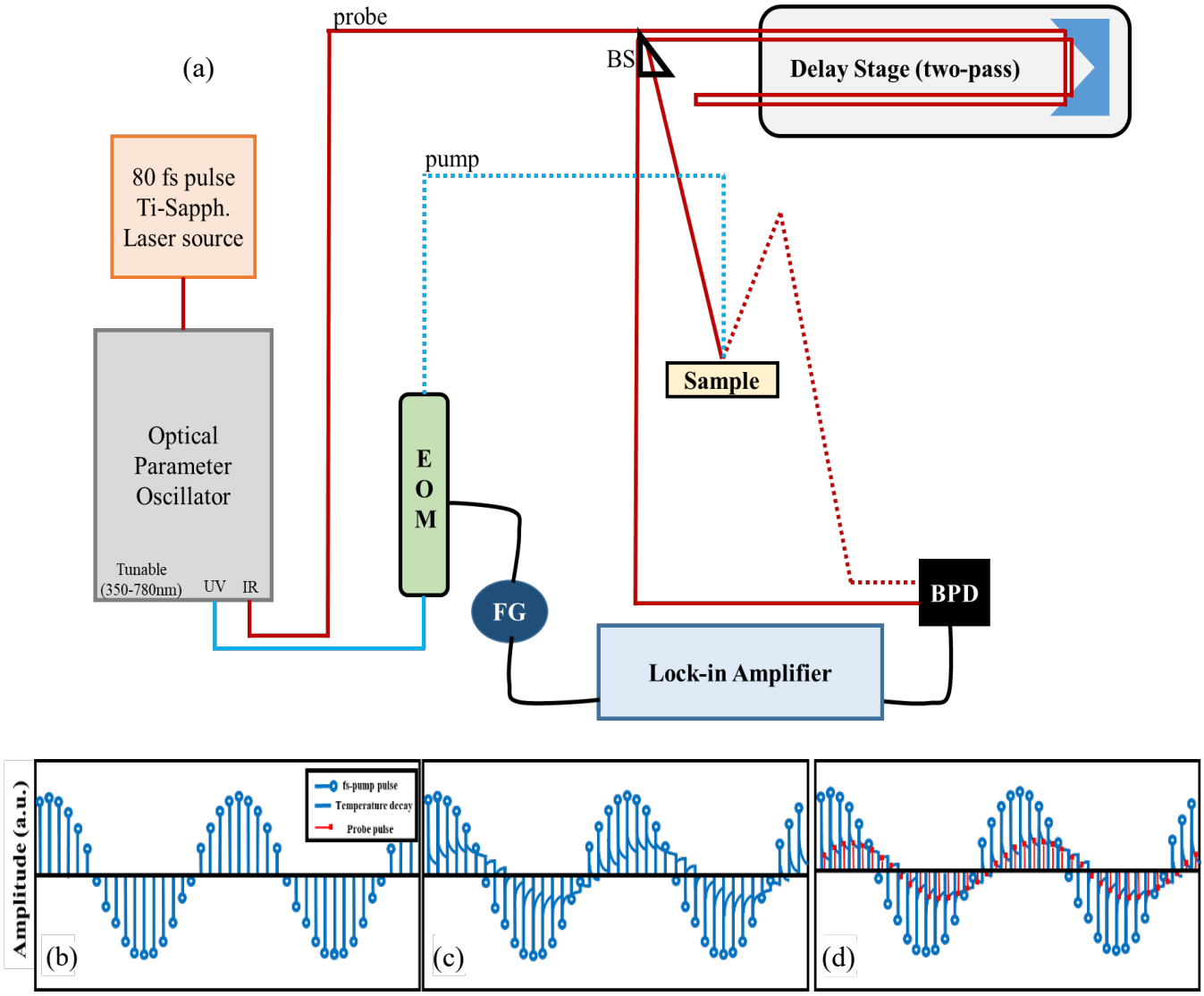

Figure 21. The schematic of the experimental set-up is shown in (a). The sine wave functions correspond to the pulse (b), the decay (c), and monitored decay (d).

For testing, since the high-temperature phase of this material is liquid, TDTR was performed by probing through the back of the glass slide substrate with the evaporated aluminum. A similar strategy was used by Schmidt et al. (2008) to determine thermal

conductivity of liquids[24]. Figure 22 depicts the sample configuration used to investigate the thermal conductivity of the sample materials, including the interfaces between both the aluminum and glass and the aluminum and material. The heat transfer model used in this case is a bidirectional heat transfer model used by Schmidt et al. (2008), which accounts for heat transfer traveling upstream from where the laser is absorbed, as well as downstream[24].

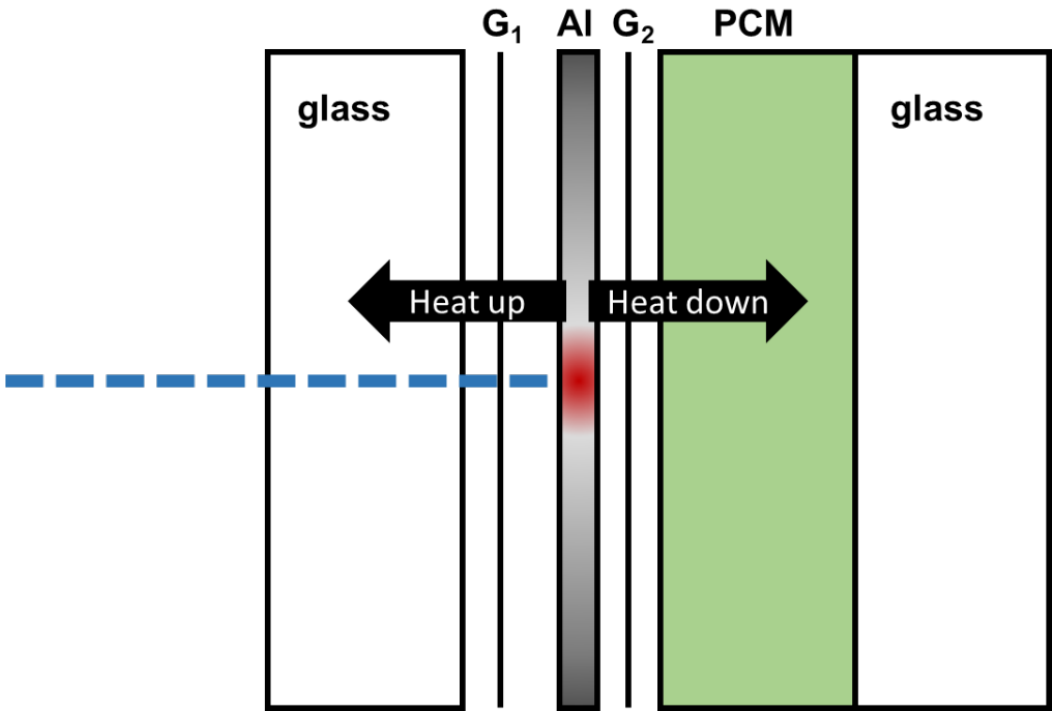

Figure 22. A schematic of bidirectional heat transfer problem and the backside probing orientation.

Owing to periodic strain, which arises due to local heating at the position where the laser is absorbed, Brillouin scattering occurs, which makes the data more difficult to fit with standard conditions. Therefore, three samples were fitted at delay times between 1 ns and 4 ns, which corresponds to the end of the delay stage. Figure 23 reports the raw data, as measured at the lock-

in amplifier, in terms of ratio of in-phase to out-of-phase components of the output voltage. In this case, 4370 m/s in good agreement with reported values of 3800 m/s[32].

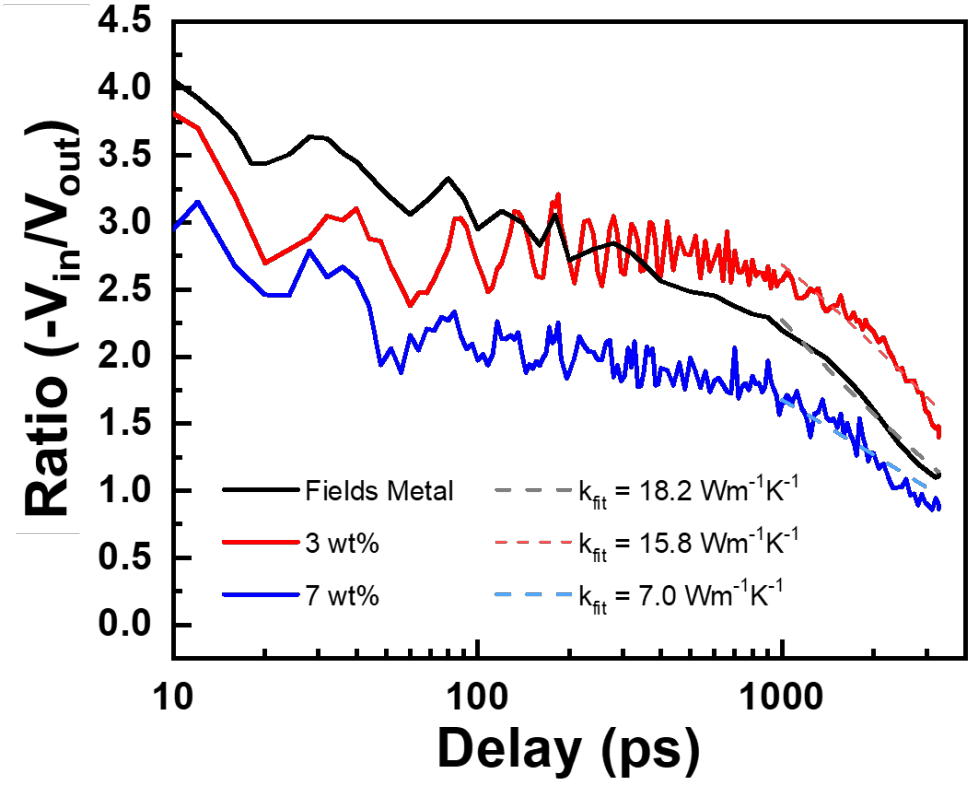

Figure 23. Ratio of in-phase to out-of-phase components of TDTR signal and model fits for Fields metal with varying concentrations of paraffin spheres.

Overall, the measurements from the TDTR systems confirm the thermal conductivity for the Field's metal sample is 18.0 W/m K. For the composite systems of 21.83% and 40.32% encapsulated paraffin wax concentrations, the measured thermal conductivities are 15.6 W/m K and 7.0 W/m K, respectively. From the assigned thermal conductivity values, an explicit system of the composite material was effectively modeled. In literature, paraffin has a recorded thermal

conductivity of 0.2 - 0.4W/m K[12]. The Field's metal was fit to the expected value of ~18.0 W/m K. Thus, the thermal conductivities of the composite system show a consistent trend of a lower sample conductivity based on the increased concentration of the organic PCM.

Chapter 5: Computer Modeling and Simulations

Army Research Laboratory's ParaPower

In order to supplement the physical testing results, an explicit model was created to analyze the relationship between the composite materials, individual material interactions, and the melting propagation fronts. The numerical computer modeling simulations were computed with the U.S. Army Research Laboratory's ParaPower software. ParaPower is a parametric modeling tool, which was co-developed by the U.S. Army Research Laboratory and the U.S. Naval Academy to enable co-design of electrical packages and an understanding of the tradeoffs across the electrical, thermal, and mechanical domains. The model uses a 3D thermal resistance network to quickly calculate the temperatures and stresses in any rectilinear geometry[4]. This transient thermal tool provides background computational modeling support. The advantage of using this tool over conventional numerical types of interactive solving software such as, ANSYS Workbench or COMSOL Multiphysics Modeling Software, relates to ParaPower's comparative computational solution response being 100 times faster.

The structure of the model is comprised of simple node temperatures and stress outputs. However, the current version of ParaPower is oriented in cubic volumetric parameters. All parameters are defined as a feature, which are then subdivided into elements comprising a 3D resistor network. The TDTR and DSC measurements supplied the information for the material data, including the solid and liquid phase properties of the microencapsulated paraffin wax and Field's metal. The properties were thermal conductivity, density, latent heat, and melting temperature.

Square vs Sphere Geometry Comparison

One challenge to overcome while using ParaPower relates to the cubic parameters associated with the model's structure. The synthesized organic materials were spherical. Paraffin particle diameters were chosen from 1-30 µm to represent the design parameters for the simulated spherical geometries. The same dimensions were chosen for the length of the particles represented as cubes. Table 11 compares the equations for the surface area and volume calculations for each geometry.

Table 11. To determine the surface area and volume of each geometry, the fundamental equations were used in the table below. The variable (l) represents a cube's side length and (d) equals the diameter of the sphere.

Fundamental Equations for Surface Area and Volume Calculations	
Surface Area of a Cube	$6*l^2$
Volume of a Cube	l^3
Surface Area of a Sphere	$4*\pi*(\frac{d}{2})^2$
Volume of a Sphere	$(\frac{4}{3})*\pi*(\frac{d}{2})^3$

The particle diameters were plotted to determine the corresponding surface area and volume values. The overlapping points at 20 µm were compared since this was the average paraffin particle size according to Microtek Laboratories, Inc. The graph of the surface area and the volume of the geometries can be seen in Figure 24 and Figure 25.

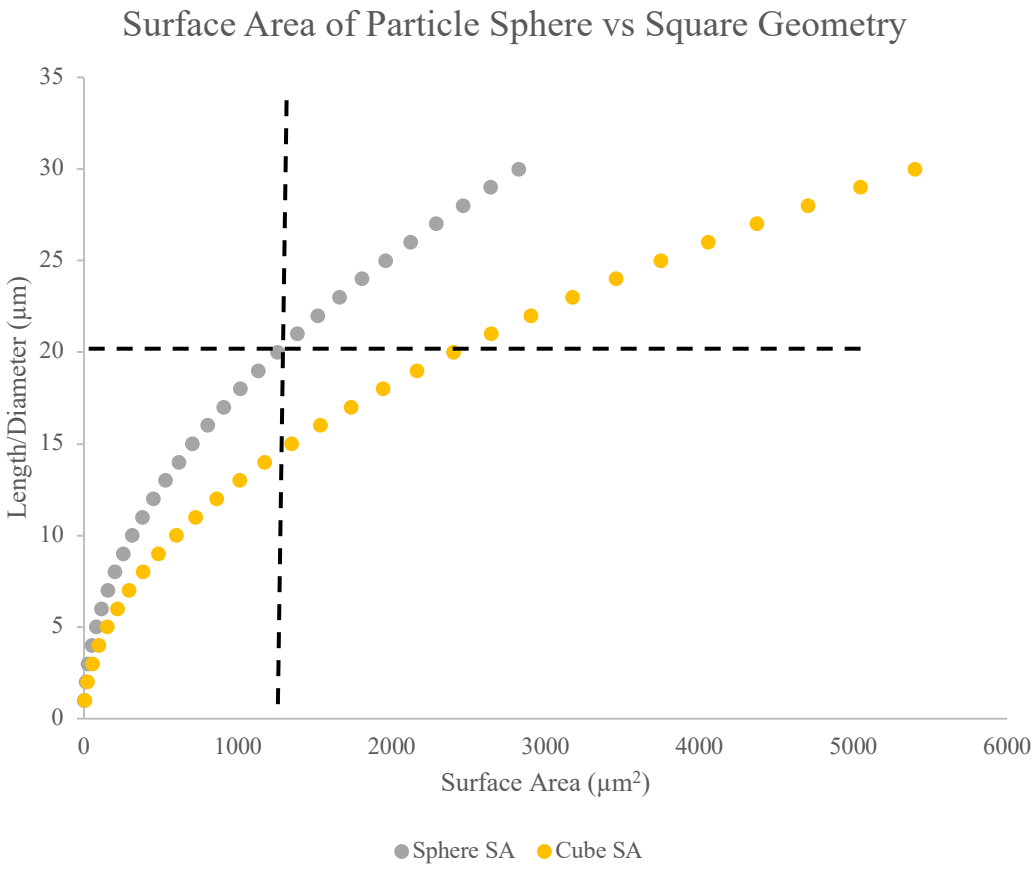

Figure 24. This graph shows the surface area of a spherical particle in comparison to the surface area of a cubic particle. The black dashed lines form a cross section corresponding to the sphere diameter of 20 µm. For the spherical geometry, the corresponding surface area is 1256 µm^2. For the cube length of 14.5 µm, the corresponding surface area is 1350 µm^2.

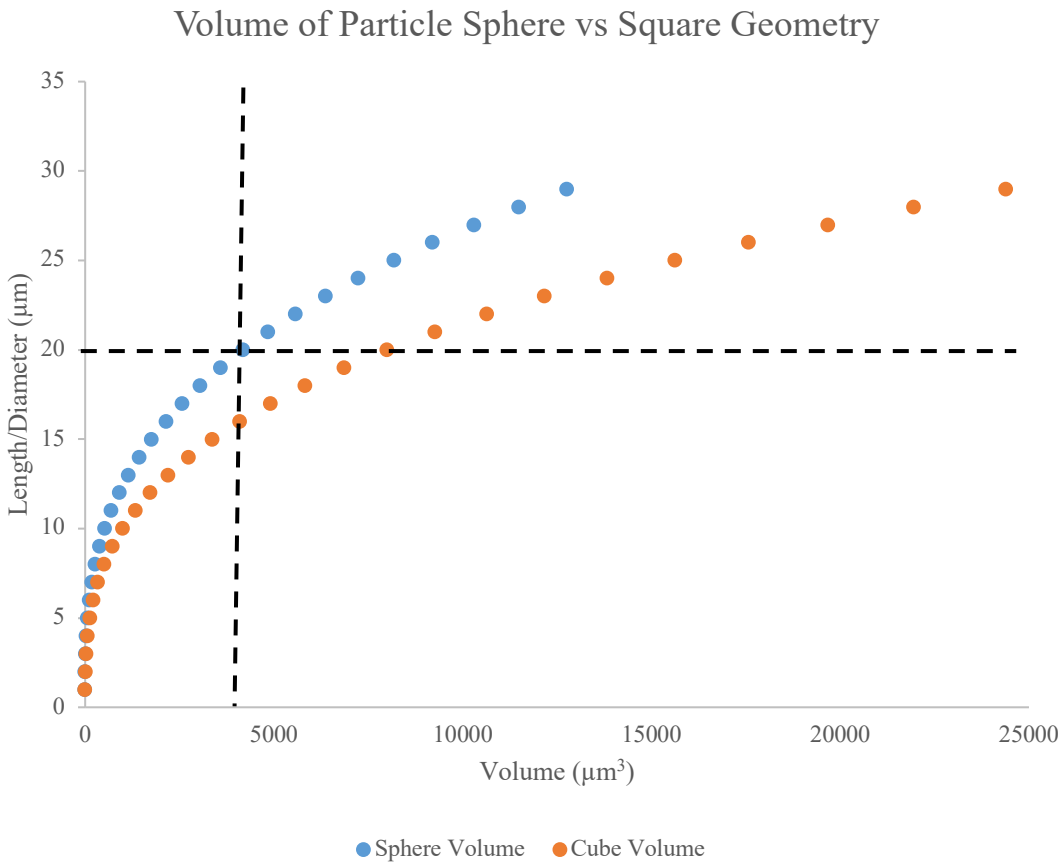

Figure 25. This graph shows the volume of a spherical particle in comparison to the volume of a cubic particle. For the spherical geometry, the corresponding volume is 4187 μm^3. For the cubic geometry of length 16 µm, the corresponding surface area is 4096 μm^3.

Spheres are the most efficient known shape in three dimensions for volume per unit surface area. In comparison, cubes are less efficient. Thus, if a cube has the same area, then the sphere will have more volume. After comparing the surface area and volume of both of the geometries, the volume parameter was chosen for the simulation comparison. To accurately model the complete spherical shape, the entire volume must be included. A comparable square of the same volume was smaller than the respective sphere. For a sphere diameter of 20 µm, the length of the cube was equal to 16 µm based on the volume fraction shown in Figure 25. This relationship

allowed the computer models to account for the interactions between the simulated, larger spheres touching one another with the void space between each particle comprising of the metallic phase change material with the cubic geometry.

Explicit Composite Model

To qualitatively track the dynamic behavior of the composite, the simplified explicit domain included the individual paraffin particles in the meshed metal resting on chip. Below the chip was a heater. The primary objective was to show the interactions between the size of the particles (µm), heat flux (W/m^2), packing density, and heat propagation through the system. The primary design focus was to obtain a qualitative picture of dynamic behavior. The thermal properties were input into the model from the TDTR and DSC measurements. The model itself was based on the principles of the heat equation with corresponding variables explained in Table 12:

$$\rho(\vec{x},T)cp(\vec{x},T)\frac{\partial T}{\partial t} = \nabla \cdot -k(\vec{x},T)\vec{\nabla}T \ .$$

Table 12. The heat equation evaluates how heat evolves over time in a solid medium as it spontaneously flows between areas of high and low temperatures. For a variable reference chart for the heat equation, see the table below.

Heat Equation Variable Reference Chart	
$\rho(\vec{x},T)$	Density [kg*m^3]
$cp(\vec{x},T)$	Specific Heat [$\frac{J}{kgK}$]
∇	Energy generated per unit volume [W*m^3]
$k(\vec{x},T)$	Material Conductivity [$\frac{W}{mK}$]
$\vec{\nabla}T$	Temperature gradient [$\frac{K}{m}$]

The explicit analysis focused on a uniform, cubic-close packed unit cell structure with ~20%, ~40%, ~50%, ~60% volume fractions of the particles. The physical concentration of the samples varied from 21.8%-61.2%. The MATLAB script can be found in Appendix F.

Heat was applied to a chip at the bottom of a 1 mm tall PCM composite. The heat propagation through the system could be analyzed by the individual material (paraffin or Field's metal) or the entire composite. Depending on the heat flux and particle size, the two materials would have different heat dissipation responses. Figure 26 shows the temperature gradient in the simulation.

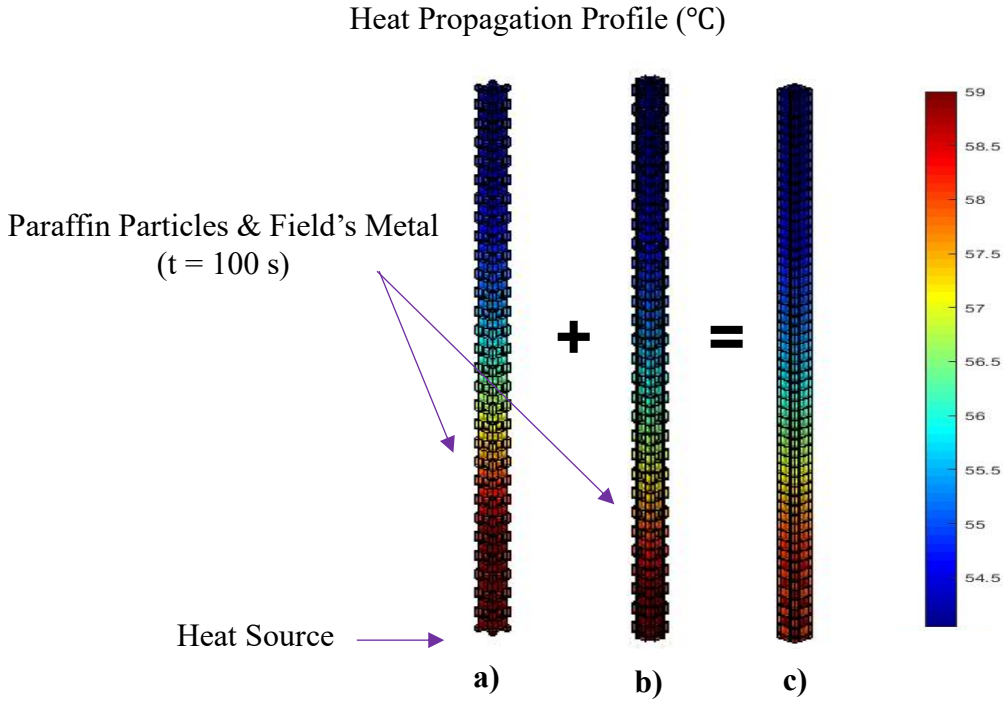

Figure 26. At a paraffin volume fraction of ~ 40%, the organic PCM (a) combines with the metallic PCM (b) to form the composite material (c). The 30 W/cm^2 heat flux is applied to the bottom of the composite system and rises. If the materials were separated, the heat propagation through each material differs as shown by the temperature gradient provided on the right side of the figure.

To avoid the overlapping of particles, the volume fractions were limited to 50% due to modeling constraints related to converting the spheres to cubic particles. However, this parameter was adjusted by altering the packing fraction and overall square geometry. Each particle changed from a cube to a cubic pixel sphere. The aspect ratio (the width to the height of the paraffin image) of sphere shape was between 0 and 1. Figure 27 shows the change in particle shape. The change in paraffin particle shape also increased the steady state delay time as shown in Figure 28.

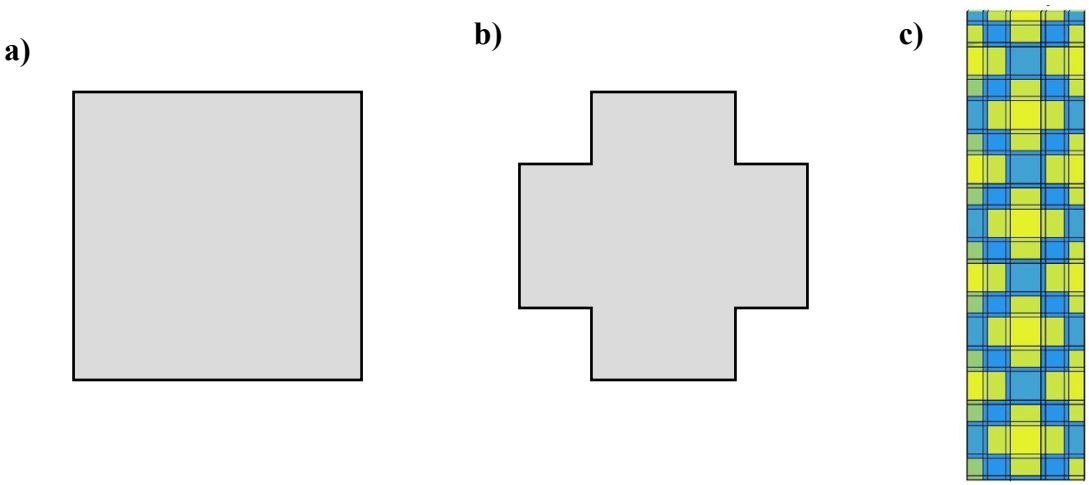

Figure 27. The cubic geometry (a) was altered to allow for higher packing fractions without corner overlap with the “plus” shape (b). The yellow “plus” paraffin particles were oriented within the column of blue Field’s metal as shown in (c).

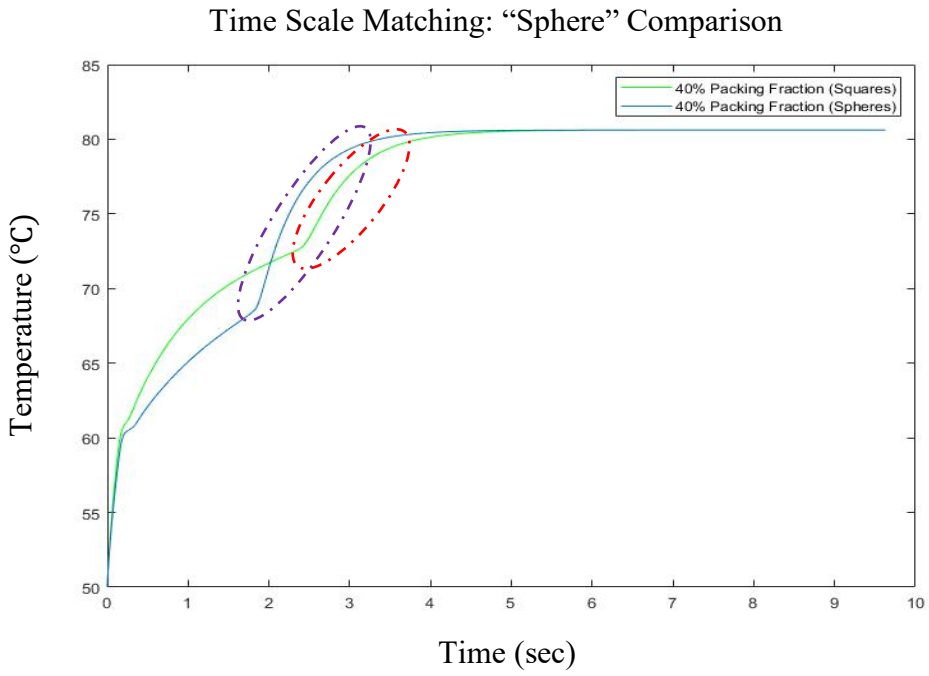

Figure 28. Graph of the heat propagation through the PCM composite with the cubic and the “plus” shape geometries under the same operating conditions. The heat flux was 30 W/cm^2 over a time step of 5000. Each particle size was 16 µm. With the “plus” shape, the completely melted regime in the dotted ovals is delayed by approximately 0.5 seconds. The steady state temperature of 80℃ is delayed by approximately 0.25 seconds.

The explicit model provided insight into the material interactions and heat propagation characteristics within the PCM composites. If tuned correctly, the model can predict specific trends at different temperatures. All final models include the “plus” paraffin geometry to account for the 61.2% volumetric fraction of the physically tested PCM composites. The importance of the particle geometry and the explicit model results are quantified in the following timescale matching section.

Timescale Matching Results

In the explicit model, the heat transfer process is broken down into 5 distinct regimes after a thermal pulse is initiated: (1) sensible heating of both the metallic PCM and organic PCM, (2) melting of the metallic PCM, sensible heating of the organic PCM, (3) melting of the metallic PCM and organic PCM, (4) sensible heating of the liquid metallic PCM and melting of the organic PCM, and (5) sensible heating of the liquid metallic PCM and organic PCM[4]. Since the two separate PCM materials can absorb different portions of the pulse based on their specific thermal properties, a time delay before reaching steady state was achieved for all four PCM composite samples compared to traditional material encapsulates. The four PCM composite samples, dielectric gel, copper, heptacosane (non-encapsulated paraffin wax), and Field's metal samples are simulated in a 1 mm block of material above a chip deposited on a heat source for a timeframe of 10 seconds. The input heat flux is 30 W/cm^2. The time step is 5000 and the paraffin particle size is 16 μm. The material comparison graph is shown in Figure 29 and is the product of the MATLAB code in Appendix F. Of particular interest for the resulting data is the time delay in heat propagation through the system between the PCM composites and copper. Copper has a high thermal conductivity of 385 W/m K and is traditionally the preferred material for heat dissipation. However, it is a very dense, solid metal compared to the lighter weight PCM composites fabricated in this study. The separation within a singular curve of the organic and metallic constituents of the PCM composites is not reflected in the graph. The melting of these samples is viewed as a uniform sample, but the individual thermal properties are maintained.

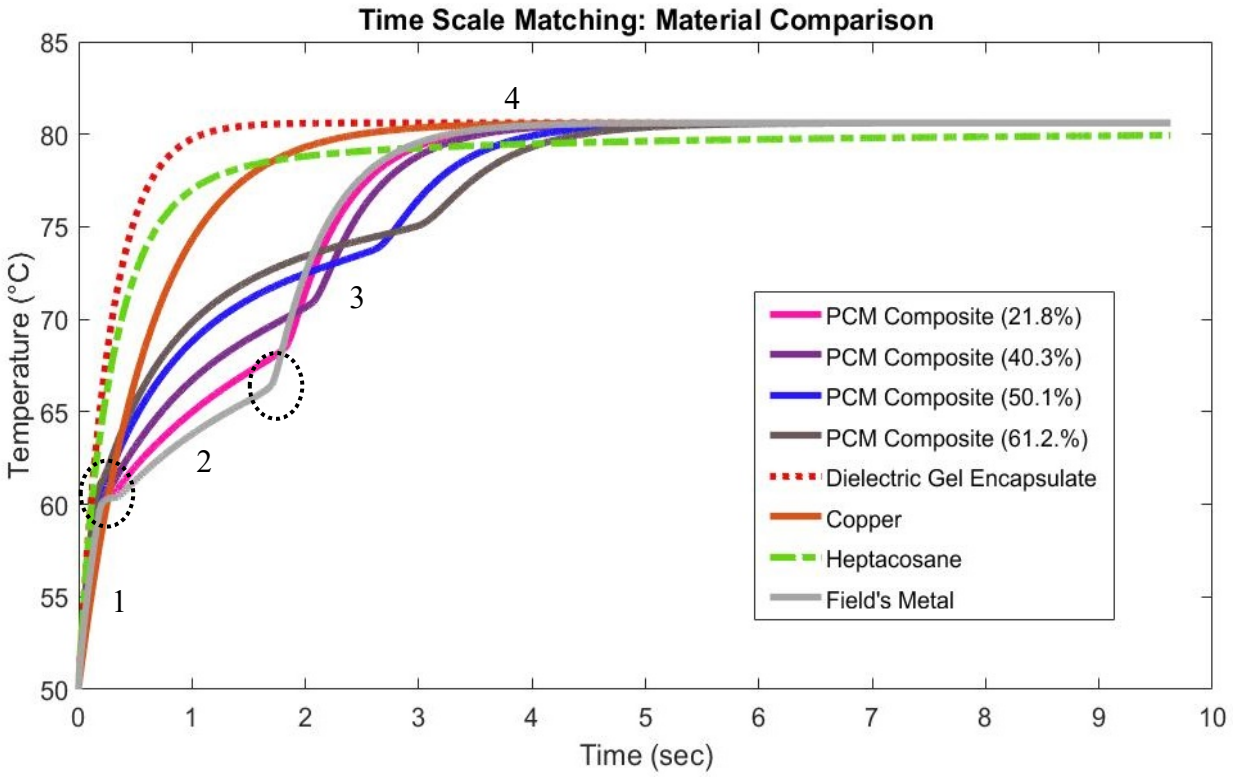

Figure 29. A comparison of different heat dissipating materials is shown. The region of the graph labeled 1 is the chip temperature heating up as the flux is applied. The dotted circle between regions 1 and 2 indicates the onset of melting for the PCMs. Region 2 is the melting of specifically Field's metal. This is the isothermal region of the graph; thus, a less steep slope is produced. The next inflection point between regions 2 and 3 indicates a completely melted PCM. Region 3 corresponds to the liquid material increasing in heat since the phase transition is no longer viable. Region 4 is the steady state for all materials for the remainder of the pulse at 80℃.

Copper reached the steady state regime at 2.55 seconds after the pulse commencement. The 21.8%, 40.3%, 50.1%, and 61.2% PCM composite samples were delayed by 26.8%, 36.3%, 43.3%, and 49.0% respectively compared to copper. This time delay is even greater compared to the dielectric gel, which simulates nearly zero material heat dissipation. By comparing the

highest paraffin concentration composite (61.2%) to the pure Field's metal, over a 1.0 second delay occurred between the completely melted second inflection points. This shows that the higher concentration of paraffin spheres did not hinder the performance of the composite systems. Even the lowest PCM composite edged the time delay of the pure Field's metal. The heptacosane served as a reference for a completely organic PCM encapsulate. Overall, the timescale matching comparison showed that the highest PCM composite had the longest duration of heat absorption before reaching the steady state of 80℃.

Chapter 6: Discussion of Results and Conclusion

The research inquiries driving this thesis work were to determine if an organic and a metallic PCM can be effectively combined to create a composite. This PCM combination must be able to be characterized physically and computationally, be supported with computer simulations, and quantitively outperform traditional PCM materials based on a heat propagation comparison in a high pulse rate transient system. If a synthesized composite consisting of an organic and metallic PCM can be fabricated, effectively characterized, and provide thermal benefits that outperform existing heat dissipation materials, then a new category of PCM composite has been achieved. Within this study, those parameters have been analyzed, supported, and accepted.

Physical Composite Testing

The physical distribution of spherical organic PCM inside a metallic substrate was physically and computationally analyzed. The organic constituents, microencapsulated paraffin wax ($T_m \sim 58°C$), were embedded into a Field's metal (32.5Bi/51In/16.5Sn wt%) ($T_m \sim 59°C$) substrate. Various mixing techniques, particle size filtration investigations, and mixing apparatuses were considered to determine the optimal organic particle dispersion within the metallic PCM. Four techniques were explored to determine a procedure that was easily replicable, could scale with varying quantities of each composite, was inexpensive, and provided consistency between samples. Manually mixing the two materials proved the most effective method to create the composite material with paraffin volumetric fractions of 21.8%, 40.3%, 50.1%, and 61.2%. By increasing the amounts of paraffin particles, the composite PCM became more viscous. The 61.2% volumetric fraction was chosen as the practical upper limit of the composite samples. The 21.8%, 40.3% and 50.1% experienced a similar physical phase change

phenomenon from solid to liquid. The 61.2% sample was a coarse solid, even under increased temperature conditions.

Two supporting homogeneity studies and corrections in the computer simulations accounted for the disperse orientations of particles in the PCM composite. The SEM images exposed morphologies in the particle shapes and nonuniform metallic particle coatings post mixing. Particles as small as 1.5 μm and as large as 44 μm were measured. The average spherical particle size was estimated to be 20 μm. In order accurately model the heat dispersion through the composite and confirm the accuracy of the conversion of mass to volumetric fraction calculation, an interior cross-sectional analysis was conducted with a micro-CT x-ray imaging technique. For each PCM composite, the averaged mico-CT volume fraction yielded an error analysis of 25.8% $\pm$ 1.26, 44.5% $\pm$ 2.18, 55.1% $\pm$ 1.47, and 64.2% $\pm$ 8.84. This was a difference of 4.0%, 4.2%, 5.0%, and 3.0% for the 21.8%, 40.3%, 50.1%, and 61.2% respective samples.

To adequately quantify the thermal properties, the latent heat of fusion, peak melting temperature, phase change onset, and thermal conductivity of each sample was measured. Pure Field's Metal had a latent heat value of 49.9 J/g, while the average was 47.0 J/g. The average latent heat for the paraffin constituents was 252.3 J/g. In literature, the latent heat obtained from DSC heating runs for Fields metal is 25.4 J/g [21] and pure paraffin wax is 259 J/g[12]. Despite the deformation in shape with the higher concentration of microencapsulated paraffin wax, the phase onset temperature and peak melting temperature remained consistent across the five samples. The average melting onset temperature was 58.2°C for Field's metal. The average onset temperature for the microencapsulated paraffin was 48.2°C. Both of these values are within 0.1°C across all five samples. The average peak temperature for the Field's metal melting curves

was 61.3°C, while the average temperature for the organic PCM was 55.9°C. Overall, the measurements from the TDTR systems confirmed the thermal conductivity for the Field's metal sample is 18.0 W/m K. For the composite systems of 21.83% and 40.32% encapsulated paraffin wax concentrations, the measured thermal conductivities are 15.6 W/m K and 7.0 W/m K, respectively. From the assigned thermal conductivity values, an explicit system of the composite material was effectively modeled.

Computer Modeling

In order to supplement the physical testing results, an explicit model was created to analyze the relationship between the composite materials, individual material interactions, and the melting propagation fronts. The explicit analysis focused on a uniform, close-packed unit cell structure with ~20%, ~40%, ~50%, ~60% volume fractions of the particles. From the model, the four PCM composite samples, dielectric gel, copper, heptacosane (non-encapsulated paraffin wax), and Field's metal samples were simulated in a 1 mm block of material above a chip deposited on a heat source for a timeframe of 10 seconds. The input heat flux was 30 W/cm^2. The time step was 5000 and the paraffin particle size was 16 μm. The 21.8%, 40.3%, 50.1%, and 61.2% PCM composite samples were delayed by 26.8%, 36.3%, 43.3%, and 49.0% respectively compared to copper. This shows that the higher concentration of paraffin spheres did not hinder the performance of the composite systems. Even the lowest PCM composite edged the time delay of the pure Field's metal. Overall, the timescale matching comparison showed that the highest PCM composite had the longest duration of heat absorption before reaching the steady state of 80℃.

Research Impact

The versatile PCM composites can be designed for specific application parameters due to their customizable organic to metallic PCM ratios, tailorable material properties, and system-specific phase change onset temperatures. The concentration of the organic PCM can be adjusted based on constraints related to the overall composite cost or weight. PCM composites can be chosen based on their thermal and physical properties for the specific application, paying particular attention to the system's temperature range. This PCM composite fabrication study is the first to combine an organic and metallic PCM together in current existing literature. The values and design set-up produced from the explicit model can be supplemented in future work with a two-temperature finite difference model.

Future Endeavors

For future work, DSC calibrations should be made for further analysis of the thermal parameters. The specific heat of the samples can be measured in regard to a reference material, specifically sapphire. This will supplement the current data with a parameter that determines the heat required to raise the temperature of the unit mass of the PCM composite by one degree Celsius. Also, the organic PCM orientation within the Field's metal can be further investigated for a more close-packed structure, as in the explicit model. A new fabrication technique could be used to create a matrix structure of fixed alignment during phase change. A computer modeling software that is able to incorporate spherical shapes would also increase the accuracy of the composite system instead of converting spherical geometries into cubic.

An additional computer model tracking the changing phase and temperature of each organic particle in relation to the surrounding Field's metal is currently being investigated at the Army Research Laboratory. In general, an effective medium model with only a single temperature

degree of freedom is unlikely to capture the full range of dynamic responses. Thus, a two-temperature model can track distinct matrix and particle temperatures at each point in the specified domain. At each point, there are four states incorporating two temperatures. Validation studies between the consistency in the outputs of the two temperature and the explicit model can aid in the creation of a data base for organic and metallic PCM combinations that can identify specific combination ratios for exact application temperature parameters. The PCM composite system can be applied in applications from solar energy, to mobile devices, to military purposes pertaining to high pulse rate lasers. The potential is limitless.

References

[1]Abdin, Z., & Khalilpour, K. R. (2019). Single and Polystorage Technologies for Renewable-Based Hybrid Energy Systems. *Polygeneration with Polystorage for Chemical and Energy Hubs*, 77–131. doi: 10.1016/b978-0-12-813306-4.00004-5

[2]Barako, M. T., Weisse, J. M., Roy, S., Kodama, T., Dusseault, T. J., Motoyama, M., … Goodson, K. E. (2014). Thermal conduction in nanoporous copper inverse opal films. *Fourteenth Intersociety Conference on Thermal and Thermomechanical Phenomena in Electronic Systems (ITherm*). doi: 10.1109/itherm.2014.6892354

[3]Bhatt, A. (2004). *Heat Pipes for Electronics Cooling* (Unpublished doctoral dissertation). San Jose State University, San Jose, California. 1-21.

[4]Boteler, L., Fish, M., Berman, M. & Wang, J. (2019). Understanding Trade-offs of Phase change Materials for Transient Thermal Mitigation. iTherm, 2019. pp.1-39.

[5]Britannica, T. E. of E. (2015). Ester. Retrieved from https://www.britannica.com/science/ester-chemical-compound

[6]Cahill, D. G. (2004). Analysis of heat flow in layered structures for time-domain thermoreflectance. *Review of Scientific Instruments*, *75*(12), 5119–5122. doi: 10.1063/1.1819431

[7]Eslamian, M., & Zabihi, F. (2015). Ultrasonic Substrate Vibration-Assisted Drop Casting (SVADC) for the Fabrication of Photovoltaic Solar Cell Arrays and Thin-Film Devices. *Nanoscale Research Letters*, 10(1). doi: 10.1186/s11671-015-1168-9.

[8]Freund M., Csikós R., Keszthelyi, S., & Mózes G. (1982). Paraffin products: properties, technologies, applications. Budapest: Akadémiai Kiadó.

[9]Ganatra, Y., Ruiz, J., Howarter, J. A., & Marconnet, A. (2018). Experimental investigation of Phase Change Materials for thermal management of handheld devices. *International Journal of Thermal Sciences*, *129*, 358–364. doi: 10.1016/j.ijthermalsci.2018.03.012

[10]Gonzalez-Nino, D., Boteler, L. M., Ibitayo, D., Jankowski, N. R., Urciuoli, D., Kierzewski, I. M., & Quintero, P. O. (2018). Experimental evaluation of metallic phase change materials for thermal transient mitigation. *International Journal of Heat and Mass Transfer*, *116*, 512-519.

[11]Gonzalez-Nino, D., Boteler, L. M., Jankowski, N. R., Ibitayo, D., & Quintero, P. O. (2017). Voiding Effects on the Thermal Response of Metallic Phase Change Materials Under Pulsed Power Loading. *ASME 2017 International Technical Conference and Exhibition on Packaging and Integration of Electronic and Photonic Microsystems (IPACK).* 1-7. IPACK2017-74118

[12]Hassan, A., Laghari, M. S., & Rashid, Y. (2016). Micro-Encapsulated Phase Change Materials: A Review of Encapsulation, Safety and Thermal Characteristics. *Sustainability, 8*(10), 1046. doi: 10.3390/su8101046

[13] Hawlader, M. N. A., Uddin, M. S., & Zhu, H. J. (2002). Encapsulated phase change materials for thermal energy storage: Experiments and simulation. *International Journal of Energy Research*, *26*(2), 159–171. doi: 10.1002/er.773

[14]Hong, Y. (2001). *Encapsulated Nanostructured Phase Change Materials for Thermal Management.* (Unpublished doctoral dissertation). University of Central Florida, Orlando, Florida.

[15]Jankowski, N. R. & McCluskey, F. P. (2013). A review of phase change materials for vehicle component thermal buffering. *Applied Energy, 113.* 1525-1561.

[16]Kenisarian, M. & Mahkamov, K. (2007). Solar energy storage using phase change materials. *Renewable and Sustainable Energy Reviews. 11*. 1913-1965. doi: 10.1016/j.rser.2006.05.005.

[17]Krishnan, S. & Garimella, S. V. (2004). Thermal Management of Transient Power Spikes in Electronics—Phase Change Energy Storage or Copper Heat Sinks? *Journal of Electronic Packaging, 126*(3), 308–316. doi: 10.1115/1.1772411

[18]Lipchitz, A., Harvel, G., & Sunagawa, T. (2013). Determination of Specific Heat of Eutectic Indium – Bismuth-Tin Liquid Metal Alloys as a Test Material for Liquid Metal - Cooled Applications. *Applied Mechanics and Materials*, *420*, 185–193. doi: 10.4028/www.scientific.net/amm.420.185

[19]Lipchitz, A., Harvel, G., & Sunagawa, T. (2015). EXPERIMENTAL INVESTIGATION OF THE THERMAL CONDUCTIVITY AND VISCOSITY OF LIQUID In-Bi-Sn EUTECTIC ALLOY (FIELD'S METAL) FOR USE IN A NATURAL CIRCULATION EXPERIMENTAL LOOP. *23rd International Conference on Nuclear Engineering*, Chiba, Japan.

[20]Liu, Z., Sun, X., & Ma, C. (2005). Experimental investigations on the characteristics of melting processes of stearic acid in an annulus and its thermal conductivity enhancement by fins. *Energy Conversion and Management*, *46*(6), 959–969. doi: 10.1016/j.enconman.2004.05.012

[21]Manasijević, I., Balanović, L., Grgurić, T. H., Minić, D., & Gorgievski, M. (2018). Study of Microstructure and Thermal Properties of the Low Melting Bi-In-Sn Eutectic Alloys. *Materials Research*, *21*(6). doi: 10.1590/1980-5373-mr-2018-0501

[22]Otsu, N., (1979). A Threshold Selection Method from Gray-Level Histograms." *IEEE Transactions on Systems, Man, and Cybernetics. 9*(1), 62–66.

[23]Schmidt, A. J., Chen, X., & Chen, G. (2008). Pulse accumulation, radial heat conduction, and anisotropic thermal conductivity in pump-probe transient thermoreflectance. *Review of Scientific Instruments*, *79*(11), doi: 10.1063/1.3006335

[24]Schmidt, A., Chiesa, M., Chen, X., & Chen, G. (2008). An optical pump-probe technique for measuring the thermal conductivity of liquids. *Review of Scientific Instruments*, *79*(6), 064902. doi: 10.1063/1.2937458

[25]Sharar, D. J., Donovan, B. F., Warzoha, R. J., Wilson, A. A., Leff, A. C., & Hanrahan, B. M. (2019). Solid-state thermal energy storage using reversible martensitic transformations. *Applied Physics Letters*, *114*(14), 143902. doi: 10.1063/1.5087135

[25]Sharma, A., Tyagi, V., Chen, C., & Buddhi, D. (2009). Review on thermal energy storage with phase change materials and applications. *Renewable and Sustainable Energy Reviews, 13*(2), 318–345. doi: 10.1016/j.rser.2007.10.005

[27]Smith, R., Inomata, H., & Peters, C. (2013). Introduction to Supercritical Fluids - A Spreadsheet-Based Approach. *Supercritical Fluid Science and Technology,* 175–273. doi: 10.1016/b978-0-444-52215-3.00004-0

[28]Sun, F., Wang, X., Yang, M., Chen, Z., Zhang, H., & Tang, D. (2017). Simultaneous Measurement of Thermal Conductivity and Specific Heat in a Single TDTR Experiment. *International Journal of Thermophysics*, *39*(1). doi: 10.1007/s10765-017-2328-1

[29]Vo, T. Q., & Kim, B. (2015). Interface thermal resistance between liquid water and various metallic surfaces. *International Journal of Precision Engineering and Manufacturing*, *16*(7), 1341–1346. doi: 10.1007/s12541-015-0176-0

[30]Vu, N., Warzoha, R. J., Donovan, B. F., Sharar, D. J., Leff, A., Wilson, A. A., et al. (2019). Effect of gain size on the thermal properties of nickel-titanium shape memory alloys across the martensite-austenite phase transition. *18th IEEE Intersociety Conference on Thermal and Thermomechanical Phenomena in Electronic Systems (ITherm).* Las Vegas, NV.

[31]Wang, X., Chen, Z., Sun, F., Zhang, H., Jiang, Y., & Tang, D. (2018). Analysis of simplified heat transfer models for thermal property determination of nano-film by TDTR method. *Measurement Science and Technology*, *29*(3), doi: 10.1088/1361-6501/aa9e18

[32]Watson, S. K., & Pohl, R. O. (2003). Low-energy lattice vibrations of porous silica glass. *Physical Review B*, *68*(10). doi: 10.1103/physrevb.68.104203

[33]Won, Y., Barako, M. T., Agonafer, D. D., Asheghi, M., & Goodson, K. E. (2014). Mechanical and thermal properties of copper inverse opals for two-phase convection enhancement. *Fourteenth Intersociety Conference on Thermal and Thermomechanical Phenomena in Electronic Systems (ITherm).* doi: 10.1109/itherm.2014.6892299

[34]Xie, B., Cheng, W.-L., & Xu, Z.-M. (2015). Studies on the effect of shape-stabilized PCM filled aluminum honeycomb composite material on thermal control. *International Journal of Heat and Mass Transfer*, *91*, 135–143. doi: 10.1016/j.ijheatmasstransfer.2015.07.108

[35]Zhong, Y., Guo, Q., Li, S., Shi, J., & Liu, L. (2010). Heat transfer enhancement of paraffin wax using graphite foam for thermal energy storage. *Solar Energy Materials and Solar Cells*, *94*(6), 1011–1014. doi: 10.1016/j.solmat.2010.02.004

[36]Zhao, C. Y., Lu, W., & Tian, Y. (2010). Heat transfer enhancement for thermal energy storage using metal foams embedded within phase change materials (PCMs). *Solar Energy, 84*(8), 1402-1412.

Appendix A: PCM Composite Weight Calculations

Field's metal has a density of 7880 kg/m^3. To determine the weight of a 1 m^3 sample, the mass was multiplied by the density. The product of this calculation was multiplied by 1000 g to yield a weight of 7,880,000 g (W_{FM}). The same calculation was performed with the microencapsulated paraffin powder, which had a density of 876 kg/m^3. A weight of 878,000 g was found (W_{PP}). The new weight (W_C) of the composite was found with the incorporation of the composite PCM volume fraction (VF):

$W_C = W_{FM}(1\text{-}VF) + (W_{PP}*VF)$.

The percent weight reduction was found with the following equation:

$W_R = 1\text{-}(W_C/W_{FM})$.

The results from the above calculations are shown in Table 13.

Table 13. The composite weight reduction determined by the concentration of microencapsulated paraffin wax.

PCM Composite Weight Comparison		
Encapsulated Paraffin Wax	Composite Weight (W_C)	Percent Weight Reduction
21.8%	$6.3*10^6$ g	19.4%
40.3%	$5.1*10^6$ g	35.8%
50.1%	$4.4*10^6$ g	44.5%
61.2%	$3.6*10^6$ g	54.4%

Appendix B: PCM Composite Cost Comparison

The Field's Metal ingot was purchased form Rotometals, Inc., which cost $352.76/lb. Using the conversion factor of 1 lb = 453.592 g, the cost of the Field's metal is $777.71/kg. The cost per volume was calculated by multiplying the density by the cost per kg (V_{FM}).

The microencapsulated organic materials were purchased from Microtek Laboratories, Inc and cost $27.00/lb, which converts to $59.53/kg. From the same calculations from above, the cost per volume was found (V_{PP}). The new cost ($C_{composite}$) of the composite was found with the incorporation of the composite PCM volume fraction (VF):

$C_{Composite} = V_{FM}(1\text{-}VF) + (V_{PP}*VF)$.

The percent cost reduction (C_R) was found with the following equation:

$C_R = 1\text{-}(C_{Composite}/V_{FM})$.

Another metric to compare the PCM composite to an all Field's metal sample is to find the difference (C_D):

$C_D = V_{FM}$ – Composite Total Cost

The results from the above calculations are shown in Table 14.

Table 14. The composite cost reduction determined by the concentration of microencapsulated paraffin wax.

PCM Composite Cost Comparison			
Encapsulated Paraffin Wax	Composite Total Cost	Cost Reduction	Difference
21.8%	$4803720.76/m^3	21.6%	$1324608.35
40.3%	$3679626.51/m^3	40.0%	$2448702.60
50.1%	$3084160.37/m^3	49.7%	$3044168.74
61.2%	$2409703.83/m^3	60.7%	$3718625.28

Appendix C: Micro-CT High to Low Resolution Comparison

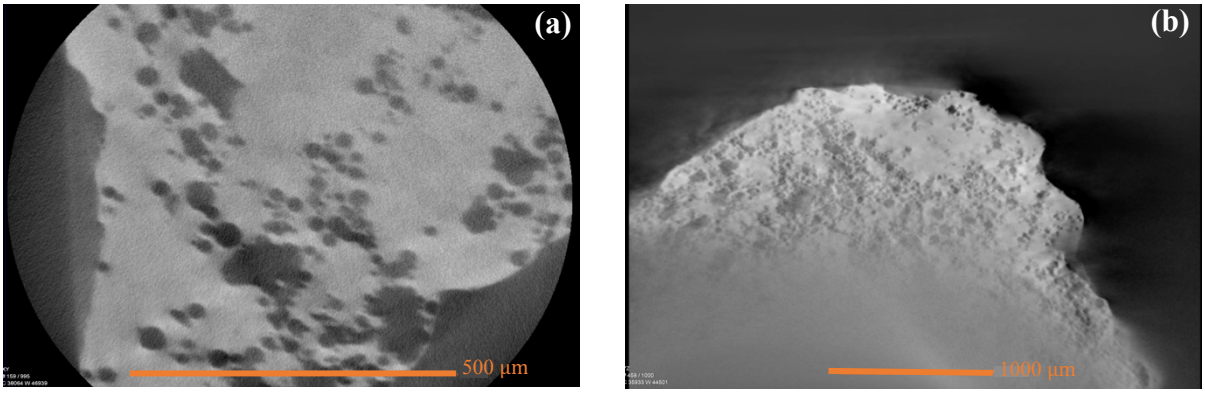

Figure 30. The 21.8% paraffin volumetric fraction sample with high resolution (a) compared to the low resolution (b).

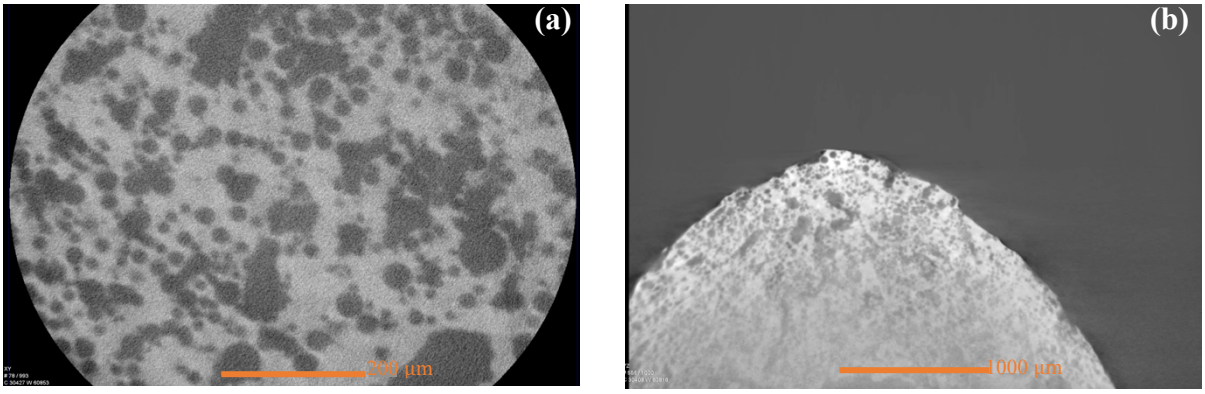

Figure 31. The 40.3% paraffin volumetric fraction sample with high resolution (a) compared to the low resolution (b).

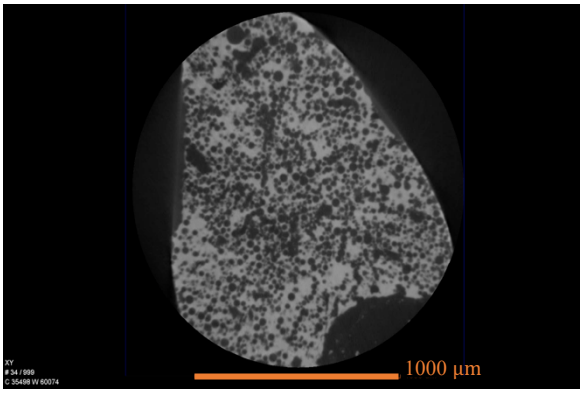

Figure 32. The 50.1% paraffin volumetric fraction was only measured with the high resolution.

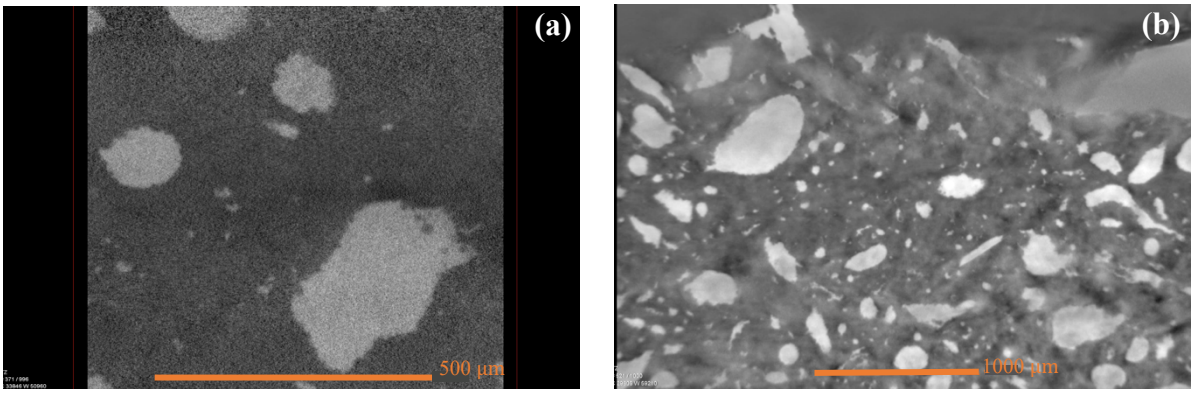

Figure 33. The 61.2% paraffin volumetric fraction sample with high resolution (a) compared to the low resolution (b).

Appendix D: Micro-CT MATLAB Code

```
v=VideoReader('/Users/MelKate/Desktop/Thesis/MicroCT/MicroCTVideos/TopVid4X.m
pg');

video=read(v);
H=size(video,1);
W=size(video,2);

video2=video(H/2+[-100:100],W/2+[-100:100],:,1:900);

gray_video=zeros(size(video2,1),size(video2,2),size(video2,4));
BW=gray_video;

for i=1:size(video2,4)
    gray_video(:,:,i)=rgb2gray(video2(:,:,:,i));
    BW(:,:,i)=imbinarize(gray_video(:,:,i)/255);
end

imshow(BW(:,:,100));

volume_frac=1-mean(BW(:,:,:),'all')
```

Appendix E: Individual Micro-CT Charts

Five still images were captured at each location from each micro-CT time-lapse video. The locations were numbered 1-5 corresponding to: 1-Center, 2-Top Right, 3-Top Left, 4-Bottom Right, and 5-Bottom Left. The shifted points move in either an x-axis or y-axis direction. The average volume fraction of each composite is shown in Tables 15–18.

Table 15. The average volumetric fraction was 25.8% ±0.013 over 300 frames. The estimated standard error within the sample was ±0.0057. From the calculated mass conversion to volumetric fraction and the micro-CT particle volumetric estimation, a difference of 4.0% was found.

21.8% Composite Micro-CT	
Location Number	Volumetric Fraction (%)
1	27.7
2	25.8
3	25.9
4	24.1
5	25.4

Table 16. The average volumetric fraction was 44.5% ±0.022 over 450 frames. The estimated standard error within the sample was ±0.0098. From the calculated mass conversion to volumetric fraction and the micro-CT particle volumetric estimation, a difference of 4.2% was found.

40.3% Composite Micro-CT	
Location Number	Volumetric Fraction (%)
1	45.3
2	42.1
3	47.6
4	42.8
5	44.7

Table 17. The average volumetric fraction was 55.1% ±0.015 over 300 frames. The estimated standard error within the sample was ±0.0066. From the calculated mass conversion to volumetric fraction and the micro-CT particle volumetric estimation, a difference of 5.0% was found.

50.1% Composite Micro-CT	
Location Number	Volumetric Fraction
1	56.3
2	53.3
3	55.3
4	56.8
5	54.1

Table 18. The average volumetric fraction was 64.2% ±0.088 over 225 frames. The estimated standard error within the sample was ±0.040. From the calculated mass conversion to volumetric fraction and the micro-CT particle volumetric estimation, a difference of 3.0% was found.

61.2% Composite Micro-CT	
Location Number	Volumetric Fraction (%)
1	65.2
2	55.0
3	55.4
4	73.7
5	71.9

Appendix F: MATLAB Explicit Model Code

```
%% Model Parameters and Material Setup

Desc='Melissa''s FCC';  %Description of the test case

h=10000;
T_fluid=50;
steps=5000;
time=9.63;
cu_h = 800e-6;
Q_flux = 30e4;
packing = 0.4;
    load('mel_mats.mat');

    MatLib.AddMatl(PPMatIBC('name'   , 'ibc_1'  ...
            ,'h_ibc'    , 0 ...
            ,'t_ibc'      , T_fluid ...
            )) ;



    %% Generate centerpoints

    %Matrix


s = 16e-6;  %in m
a = (4*s^(3)/packing)^(1/3)/sqrt(2);    % c-c dist
c = (sqrt(3)/2)*a - s;  %minimum edge-to-edge

Params.Tinit     = T_fluid;
Params.Tsteps    = steps;
Params.DeltaT    = time/Params.Tsteps;

keep_x=sqrt(2)*a; keep_y=keep_x;

keep_z= 1e-3;

Q=Q_flux*keep_x*keep_y;


x_1 = [sqrt(2)/2*a; sqrt(2)/2*a; 0];

x_2 = [0; sqrt(2)/2*a; sqrt(2)/2*a];

x_3 = [sqrt(2)/2*a; 0; sqrt(2)/2*a];


%centerpoint matrix
```

```
%latticepoint matrix

span_110=[-100:20];
span_011=[-20:100];
span_101=span_011;



lattice=zeros(3,numel(span_110)*numel(span_011)*numel(span_101));
centers=lattice;

for i=1:numel(span_110)
    for j=1:numel(span_011)
        for k=1:numel(span_101)
            ind=sub2ind([numel(span_110) numel(span_011)
numel(span_101)],i,j,k);
            centers(:,ind)=[span_110(i) span_011(j) span_101(k)]';
            lattice(:,ind)=[x_1 x_2 x_3]*[span_110(i) span_011(j)
span_101(k)]';

        end
    end
end

%figure
% scatter3(lattice(1,:),lattice(2,:),lattice(3,:),100)

 maskx=lattice(1,:)<=keep_x/2+100*eps & lattice(1,:)>=-keep_x/2-100*eps;
 %findx=find(lattice(1,:)<=keep_x & lattice(1,:)>=-keep_x);

  masky=lattice(2,:)<=keep_y/2+100*eps & lattice(2,:)>=-keep_y/2-100*eps;
   maskz=lattice(3,:)>=0 & lattice(3,:)<=keep_z;

   full_mask=all([maskx;masky;maskz],1);

   figure
 scatter3(lattice(1,full_mask),lattice(2,full_mask),lattice(3,full_mask),100)

c_pnts=lattice(:,full_mask);

%BaseFeature
    BaseFeature.x    = [-s/2 s/2];
    BaseFeature.y    = BaseFeature.x;
    BaseFeature.z    = BaseFeature.x;
    BaseFeature.dx   = 1;
    BaseFeature.dy   = 1;
    BaseFeature.dz   = 1;
    BaseFeature.Matl = 'heptacosane';
    BaseFeature.Q    = 0;

    clear Features
    Features(1:size(c_pnts,2))=BaseFeature;
    %Features(:)=BaseFeature;

    ExternalConditions.h_Xminus=0;
```

```
    ExternalConditions.h_Xplus =0;
    ExternalConditions.h_Yminus=0;
    ExternalConditions.h_Yplus =0;
    ExternalConditions.h_Zminus=h;
    ExternalConditions.h_Zplus =0;

    ExternalConditions.Ta_Xminus=20;
    ExternalConditions.Ta_Xplus =20;
    ExternalConditions.Ta_Yminus=20;
    ExternalConditions.Ta_Yplus =20;
    ExternalConditions.Ta_Zminus=T_fluid;
    ExternalConditions.Ta_Zplus =20;

    ExternalConditions.Tproc=280;

    PottingMaterial  = 0;

    %Move cubes to
for i=1:size(c_pnts,2)
    Features(i).x=Features(i).x+c_pnts(1,i);
    Features(i).y=Features(i).y+c_pnts(2,i);
    Features(i).z=Features(i).z+c_pnts(3,i);
end

%GaFeature
    GaFeature.x    = [-keep_x keep_x]/2;
    GaFeature.y    = [-keep_y keep_y]/2;
    GaFeature.z    = [0 keep_z];
    GaFeature.dx   = 1;
    GaFeature.dy   = 1;
    GaFeature.dz   = 1;
    GaFeature.Matl = 'heptacosane';
    GaFeature.Q    = 0;

    IBCFeature(1).x    = [-keep_x keep_x]/2;
    IBCFeature(1).y    = [-keep_y keep_y]/2;
    IBCFeature(1).z    = [-cu_h GaFeature.z(2)];
    IBCFeature(1).dx   = 1;
    IBCFeature(1).dy   = 1;
    IBCFeature(1).dz   = 1;
    IBCFeature(1).Matl = 'ibc_1';
    IBCFeature(1).Q    = 0;

    IBCFeature(2:4)=IBCFeature(1);
    IBCFeature(1).x=IBCFeature(1).x-keep_x;
    IBCFeature(1).y=IBCFeature(1).y*3;
    IBCFeature(2).y=IBCFeature(2).y-keep_y;
    IBCFeature(3).x=IBCFeature(3).x+keep_x;
    IBCFeature(3).y=IBCFeature(3).y*3;
    IBCFeature(4).y=IBCFeature(4).y+keep_y;

    IBCFeature(5).x    = [-keep_x keep_x]*3/2;
    IBCFeature(5).y    = [-keep_y keep_y]*3/2;
    IBCFeature(5).z    = [GaFeature.z(2) GaFeature.z(2)*1.5];
    IBCFeature(5).dx   = 1;
    IBCFeature(5).dy   = 1;
    IBCFeature(5).dz   = 1;
```

```
    IBCFeature(5).Matl = 'ibc_1';
    IBCFeature(5).Q    = 0;

 %heater
    hFeature(1).x    = [-keep_x keep_x]/2;
    hFeature(1).y    = [-keep_y keep_y]/2;
    hFeature(1).z    = [0 0];
    hFeature(1).dx   = 1;
    hFeature(1).dy   = 1;
    hFeature(1).dz   = 1;
    hFeature(1).Matl = 'NoMatl';
    hFeature(1).Q    = Q;

 %underside
    hFeature(2).x    = [-keep_x keep_x]/2;
    hFeature(2).y    = [-keep_y keep_y]/2;
    hFeature(2).z    = [-s/2 0];
    hFeature(2).dx   = 1;
    hFeature(2).dy   = 1;
    hFeature(2).dz   = 1;
    hFeature(2).Matl = 'Cu';
    hFeature(2).Q    = 0;

     %underside
    hFeature(3).x    = [-keep_x keep_x]/2;
    hFeature(3).y    = [-keep_y keep_y]/2;
    hFeature(3).z    = [-cu_h 0];
    hFeature(3).dx   = 1;
    hFeature(3).dy   = 1;
    hFeature(3).dz   = 1;
    hFeature(3).Matl = 'Cu';
    hFeature(3).Q    = 0;

full_Features=[GaFeature Features hFeature IBCFeature];

 %% Assemble Model
TestCaseModel=PPTCM;
TestCaseModel.Features=full_Features;
TestCaseModel.Params=Params;
TestCaseModel.PottingMaterial=PottingMaterial;
TestCaseModel.ExternalConditions=ExternalConditions;

TestCaseModel.MatLib=MatLib;


MI=FormModel(TestCaseModel);

%{
%we shouldnt have to do this
MI.Model(:,:,3)=18;
MI.Model(3:7,3:7,3)=1;
%}


%Visualize('Geometry',MI,'NoAxes');
```

```
%% Run simulation and Store Results
S1=scPPT('MI',MI);
[T_out,T_in,PH_out,PH_in]=S1(MI.GlobalTime);

T_res = cat(4,T_in,T_out);  %Prepend initial state
maxT=squeeze(max(T_res,[],[1,2,3]));
maxT_PT=squeeze(max(T_res(MI.Model==4),[],[1,2,3]));

PH_res=cat(4,PH_in,PH_out);  %Prepend initial state
maxPH=squeeze(max(PH_res,[],[1,2,3]));
maxPH_PT=squeeze(max(PH_res(MI.Model==4),[],[1,2,3]));


figure
plot((MI.GlobalTime),maxT)
hold on
plot((MI.GlobalTime),maxT_PT)


f_3 = figure(3);
Visualize('Temp',MI,'NoAxes','State',T_res(:,:,:,end),'RemoveMaterial',[0
18])

f_4 = figure(4);
Visualize('Melt',MI,'NoAxes','State',PH_res(:,:,:,end),'RemoveMaterial',[0
18])

f = figure();
Visualize('Temperature',MI,'state',T_res(:,:,:,100),'NoAxes');

%clear S1
%clear TestCaseModel
```